Snow albedo sensitivity to macroscopic surface roughness using a new ray tracing model

Fanny Larue[1], Ghislain Picard[1], Laurent Arnaud[1], Inès Ollivier[1], Clément Delcourt[1], Maxim Lamare[1,2], François Tuzet[1,2], Jesus Revuelto[2], Marie Dumont[2]

[1]UGA/CNRS, Institut des Géosciences et de l'Environnement (IGE), Grenoble, 38100, France

[2]Univ. Grenoble Alpes, Université de Toulouse, Météo-France, CNRS, CNRM, Centre d'Études de la Neige, Grenoble, France

Correspondence to: Fanny Larue (fanny.larue@univ-grenoble-alpes.fr)

Abstract. Most models simulating snow albedo assume a flat and smooth surface, neglecting surface roughness. However, the presence of macroscopic roughness leads to a systematic decrease in albedo due to two effects: 1) photons are trapped in concavities (multiple reflection effect) and, 2) when the sun is low, the roughness sides facing the sun experience an overall decrease in the local incident angle relative to a smooth surface, promoting higher absorption, whilst the other sides has weak contributions because of the increased incident angle or because they are shadowed (called the effective angle effect here). This paper aims to quantify the impact of surface roughness on albedo and to assess the respective role of these two effects, with 1) observations over varying amounts of surface roughness, and 2) simulations using the new Rough Surface Ray Tracer (RSRT) model, based on a Monte Carlo method for photon transport calculation.

The observations include spectral albedo (400-1050 nm) over manually-created roughness surfaces with multiple geometrical characteristics. Measurements highlight that even a low fraction of surface roughness features (7 % of the surface) causes an albedo decrease of 0.02 at 1000 nm when the solar zenith angle (Θ_s) is larger than 50°. For higher fractions (13 %, 27 % and 63 %), and when the roughness orientation is perpendicular to the sun, the decrease is of 0.03 – 0.04 at 700 nm and of 0.06 – 0.10 at 1000 nm. The impact is 20% lower when roughness orientation is parallel to the sun. The observations are subsequently compared to RSRT simulations. Accounting for surface roughness improves the model observation agreement by a factor two at 700 nm and 1000 nm (errors of 0.03 and 0.04, respectively), compared to simulations considering a flat smooth surface. The model is used to explore the albedo sensitivity to surface roughness with varying snow properties and illumination conditions. Both multiple reflections and the effective angle effect have more impact with low SSA (< 10 m^2 kg^{-1}). The effective angle effect also increases rapidly with Θ_s at large Θ_s. This latter effect is larger when the overall slope of the surface is facing away the sun and with a roughness orientation perpendicular to the sun.

For a typical alpine snowpack in clear sky conditions, a broadband albedo decrease of 0.05 causes an increase of the net short wave radiation of 80 % (from 15 W m^{-2} to 27 W m^{-2}). This paper highlights the necessity to consider surface roughness in the estimation of the surface energy budget.

1 Introduction

Spectral albedo quantifies the proportion of solar energy reflected by a surface for each wavelength, and governs the quantity of solar radiation absorbed in the snowpack. Because snow has an overall high albedo in the solar spectrum, a small decrease in albedo (e.g. from 0.85 to 0.75) drastically increases the proportion of absorbed energy (from 25% to 15% ; Genthon, 1994). Thus, a reduction in albedo has important consequences on the surface energy budget, impacting surface temperature (Mondet and Fily, 1999, Picard et al. 2012, Fréville et al., 2014), and the hydrology of watersheds (e.g. Flanner et al., 2009; Painter et al., 2010; Oaida et al., 2015). Several studies have investigated the spatial and temporal variability of snow albedo using in-situ data (Brock et al., 2000; Wuttke et al., 2006; Dumont et al., 2017) or satellite observations (Atlaskina et al., 2015; Naegeli & Huss, 2017). Snow spectral albedo generally depends in a complex way on several factors, including 1) the snow physical

40 and chemical properties, mainly the Specific Surface Area of snow grains (SSA, Gallet et al., 2009) and the concentration of light absorbing particle (LAP, Skiles et al., 2018), 2) the spectral and angular characteristics of the incident radiation (Warren, 1982), 3) the presence of macroscopic surface roughness (Kuhn, 1985; Warren et al., 1998; Mondet and Fily, 1999). The first two points have been thoroughly studied, showing that for a smooth surface, snow albedo decreases as SSA lowers (coarsening snow granularity) and with a higher sun elevation (i.e. a decrease in solar zenith angle), both of which lead to an increased

45 absorption (Warren et al., 1998, Kokhanovsky and Zege, 2004). Nevertheless, the effects of roughness are often neglected due to the difficulty to characterise the actual surface roughness within the footprint of the sensor.

Snow-covered surfaces often exhibit macroscopic roughness, resulting from snow transport or erosion by the wind or snow melting (Filhol and Sturm, 2015). In Antarctica, roughness height ranges from a few centimetres to a few meters (Warren et al., 1998; Wuttke et al., 2006), and the features' axis is usually aligned along the prevailing wind direction (Furukawa et al.,

50 1996), whereas in alpine areas the spatial distribution of macroscopic roughness mainly depends on topography, which drives wind direction and its intensity (Naaim-Bouvet et al., 2011). Kuhn (1974) was the first to report a reduction of the forward peak of the Bidirectional Reflectance Distribution Function (BRDF) over a sastrugi field, and attributed this fact to shadows when the solar azimuth angle is perpendicular to the sastrugi. This motivated further studies that showed a systematic albedo decrease in presence of roughness (Caroll and Fitch, 1981; Leroux and Fily, 1998; Corbett and Su, 2015). The amplitude of

55 the reduction in albedo depends on illumination conditions, snow properties, the size and the orientation of roughness features (Hudson and Warren, 2007; L'Hermitte et al., 2014). For instance, in high altitude mountain glaciers, the presence of penitentes, which can reach several meters in height (Lliboutry, 1953), causes a measured albedo decrease of 8-10% (Corripio and Purves, 2006). These studies underlined the difficulty of precisely quantifying the impact of roughness since the illumination conditions and snow properties also vary during albedo measurements, making it difficult to evaluate the reduction in albedo due to

60 roughness only. A protocol was proposed by Kuchiki et al. (2011) using a controlled environment where the precise roughness shapes, orientation and dimensions, snow properties and illumination conditions were known. Over a manually-created artificial roughness field, they showed that the hemispherical-directional reflectance (HRDF) factor varies by more than ± 50% relative to a smooth surface. Nevertheless, they did not acquire albedo measurements, i.e. bi-hemispherical reflectance.

Warren et al. (1998) showed that the albedo decrease over a roughness field is controlled by two effects: 1) a decrease in the

65 insolation-weighted average incidence angle relative to a flat surface (further referred to as the effective angle effect), and 2) multiple reflections in the concavities. The first effect is explained by the fact that the sides of the roughness shapes facing the sun experience stronger radiation with a smaller angle than the solar zenith angle which enhances absorption in the case of snow surface (Warren, 1982), and the sides facing away from the sun receive less radiation due to shadows or grazing angles. The insolation-weighted average albedo is therefore reduced relatively to a flat and smooth surface (Warren, 1982; 1998;

70 Kokhanovsky and Zege, 2004). The effective angle effect varies with the shape, size, and orientation of the roughness features (Carroll and Fitch, 1981; L'Hermitte et al., 2014), and is significant under direct illumination and for low sun elevations only (Warren et al., 1998). The second effect of roughness involves multiple reflections cause by the trapping of photons between roughness shapes (Pfeffer and Bretherton, 1987). Over a smooth surface, a photon only hits the surface once and is either absorbed or reflected to the sky. Over a rough surface, photons can not only be absorbed or reflected to the sky, but they can

75 also be reflected back to the surface. In this latter case, they have another probability to be absorbed, at every hit. This results in a systematic increase in absorption, and thus a decrease in albedo. The impact is maximal when the probabilities of reflection and absorption are balanced, i.e. for intermediate values of albedo (close to 0.5 in the near infrared at 700-1100 nm). Instead in the visible where albedo is close to 1, the probability of absorption is too low to trap the photons, and oppositely in the mid-infrared where the albedo is close to 0, the impact of multiple reflections is negligible. This trapping effect operates under

80 direct and diffuse illumination. Although these two effects have never been quantified separately, Warren et al. (1998) suggested to acquire measurements in diffuse illumination to estimate the impact of multiple reflections only.

Photometric models based on analytical equations were developed to simulate the effects of roughness on albedo using idealized geometric shapes (Carroll, 1982; Pfeffer and Bretherton, 1987; Wendler and Kelley, 1988; Leroux and Fily, 1998; Cathles et al., 2011; 2014; Zhuravleva and Kokhanovsky; 2010, 2011). Leroux and Fily (1998) predicted a decrease in albedo over a sastrugi field of 5 - 9 % at 900 nm, depending on the sastrugi orientation with respect to the sun position. Despite their interest to draw general conclusions on the albedo sensitivity to roughness characteristics, these models are of limited interest for real roughness features due to the idealization of the shapes (Warren et al., 1998). In addition, they use the Lambertian approximation to represent the surface reflectivity, and do not consider the intrinsic BRDF of the snow, meaning that they cannot simulate the effective angle effect. To explore the real impact of surface roughness, a 3D radiative transfer model is needed. Monte Carlo photon transport algorithms are convenient approaches (Lafortune, 1995; O'Rawe, 1991; Iwabuchi, 2006; Kuchiki et al., 2011). However, most studies using these numerical methods aim to evaluate the BRDF or HRDF instead of albedo, as their application domain was remote sensing (Kuchiki et al., 2011; L'Hermitte et al., 2014; Corbet et al., 2015).

The aims of this paper are two-fold: 1) to quantify the impact of surface roughness on snow albedo, as a function of roughness features, illumination conditions and snow properties, and 2) to assess the respective roles of the effective angle effect and multiple reflections with a new model able to represent surface roughness. Firstly, we collected albedo measurements in controlled experiments following the idea of Kuchiki et al. (2011). We produced various artificial rough surfaces during four field campaigns in the French Alps in 2018 and 2019 (Sect. 2). In each experiment, albedo measurements were acquired for several illumination conditions and with numerous geometrical characteristics at the surface. Observations were also acquired over nearby smooth surfaces to serve as references. Secondly, we developed a new model based on the Monte Carlo photon transport method, the Rough Surface Ray Tracing model (RSRT), to simulate albedo by considering surface roughness (Sect. 3). RSRT was evaluated using the albedo observations (Sect. 4.1). In Section 4.2, the model was used to explore the albedo sensitivity to surface roughness according to SSA, terrain slope, roughness orientation and solar zenith angle. The model was applied to assess the respective roles played by the effective angle effect and multiple reflections (Sect. 4.3). At last, the sensitivity of the net short wave radiation to the presence of surface roughness is discussed to estimate the potential impact on the surface energy balance (Sect. 4.4).

2 Field experiments

In situ measurements of albedo were acquired in the French Alps over smooth and rough snow surfaces. This section details how the rough surfaces were created, and measurements acquired in the field.

2.1 Artificial rough snow surfaces

Artificial rough snow surfaces were created by delineating squares of 2.5 x 2.5 m². Roughness features were manually created on natural smooth surfaces, by varying their number and orientation. The features were produced parallel to each other, regularly spaced with a period Λ, and with an azimuth angle φ_r, taken clockwise from the North. The roughness orientation with respect to the solar azimuth angle (φ_s) was defined by $\Delta\varphi_r$, the difference $\varphi_s - \varphi_r$. Figure 1 shows the experimental setup and the variables involved. Each surface was characterised by its aspect, its slope, and its roughness properties (number, shape, size and orientation). Two types of experiments were performed:

    a)   Sensitivity to the fraction of roughness features:

The fraction of roughness features in the 2.5 x 2.5 m² area is described with the width-to-period ratio η *(i.e. $\eta = W/\Lambda$,* expressed in percentage, where W is the width of roughness shapes). The albedo sensitivity to η was studied during two experiments at the Col du Lautaret site (45°2' N, 6°2' E, 2100 m a.s.l.) over two different dates (06 April 2018 and 17 April 2018), respectively called experiments A and B. Figure 2 illustrates the field experiment A, and Table 1 details the characteristics, acronyms and

parameters for each studied surface. Snow albedo was first measured over the smooth surface (called A-smooth and B-smooth-dry in Table 1), and then the roughness shapes were created in the smooth surface by uniformly pressing a rectangular metal bar into the snow (H = 2 cm depth and W = 4 cm width), in the North-South direction (φ_r = 0°-180°). The rectangular shapes were created with a period Λ = 55 cm (5 shapes over 2.5 m, η = 7 %). After albedo measurements were acquired, identical

125   rectangular shapes were added to reach a period Λ = 30 cm (10 shapes over 2.5 m, η = 13 %), then Λ = 15 cm (20 shapes over 2.5 m, η = 27 %) (Figure 2 and Table 1). Because it takes approximately one hour to make a series of measurements, the increasing fraction of roughness features is correlated to solar zenith angle (Θ_s) variations that also change albedo. To attempt to decouple the two effects, experiment A was conducted when the sun was going down (Θ_s went from 56.6° to 63.7°), whereas in experiment B, the sun was going up (Θ_s went from 56.0° to 40.0°).

130   Other changes may also occur during that time. In experiment B for instance, melting was observed on the B-$\eta27\%$ surface (the sun was close to the nadir), which leads to an increase in snow wetness and a decrease in surface SSA compared to the B-smooth-dry surface analysed at the beginning of the day. To allow more reliable comparisons, we simultaneously measured albedo over the B-$\eta27\%$ surface, and a nearby smooth surface (called B-smooth-wet in Table 1).

b) Sensitivity to the roughness orientation:

135   The albedo sensitivity to roughness orientation was studied with two experiments at the Arcelle site (45°6' N, 5°52' E, 1729 m a.s.l.) over two dates (11 January 2019 and 22 February 2019), respectively called experiments C and D. The roughness shapes were triangular, H = 6 cm depth and W = 7 cm width, and created with a period Λ = 11 cm (η = 63 %). Fig. 1b and Table 1 detail the experimental setup.

In experiment C, measurements were simultaneously acquired every 20 minutes over a surface with roughness features

140   oriented at φ_r = 90° (called C rough 90°), another one with roughness features at φ_r = 0° (called C rough 0°), and a smooth surface for reference (called C smooth). In experiment D, only two surfaces were compared every 20 minutes: a rough surface with roughness features at φ_r = 90° (called D rough 90°), and a smooth surface (called D-smooth). For both experiments, studied surfaces were close enough to consider that snow properties evolved with the same dynamics. Note that it took about up to 5 minutes to acquire one set of albedo measurements, and to move to the next surface. Measurements were acquired all

145   day in the experiment C (sun going up and down), and during the morning in experiment D (sun going up only).

The albedo sensitivity to roughness features is quantified by comparing rough and smooth surfaces for each experiment.
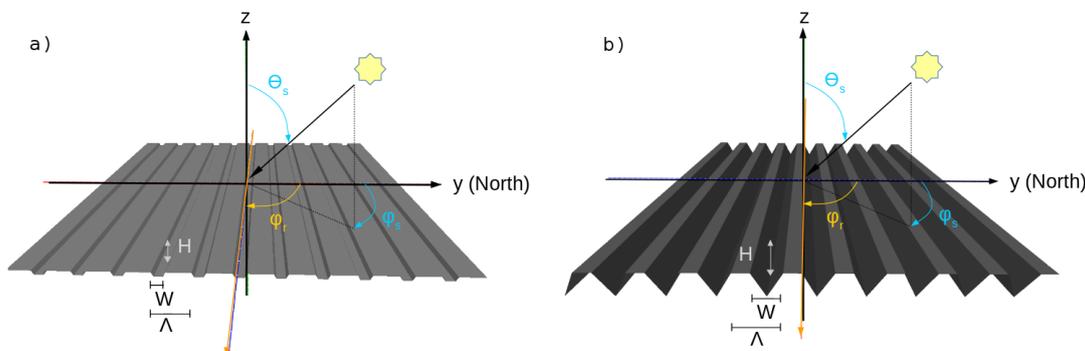
Figure 1. Illustration of the setups for a) A-η27% and B-η27% experiments, and b) C rough 90° and D rough 90° experiments (Table 1 for acronyms). The grey surfaces are modelled meshes with parallel shapes (rectangular or triangular), similar to the artificial

150   **roughness surfaces created in the field. The two sites are areas of 2.5 x 2.5 m². H is the height, W the width, and Λ the period of roughness features. φ_r is the roughness orientation, φ_s the solar azimuth angle, and θ_s the solar zenith angle. Azimuth angles are clockwise from North (y axis).**

Figure 2. Studied surfaces of experiment A (Table 1), from left to right: A-smooth, A-η7%, A-η13%, and A-η27% sites.

155   **Table 1. Details of field experiments. The sensor's height is fixed at 65 cm.**

Location	#field experiment	Acronyms	SSA [m²/kg]	$\Delta\varphi_r$ [°]	η [%]	φ_s [°]	θ_s [°]	Slope θ_n [°]	Aspect φ_n [°]	Characteristics
Col du Lautaret (April 2018)	**A**	A-smooth	7.4	-	0	242	56.6	3.1	216	Naturally flat smooth surface
		A-η7%	7.4	64	7.0	244	57.5	3.1	216	5 Rectangular shapes
		A-η13%	7.4	69	13	249	61.8	3.1	216	10 Rectangular shapes
		A-η27%	7.4	71	27	251	63.4	3.1	216	20 Rectangular shapes
	B	B-smooth-dry	4.5	-	0	112	55.5	3.6	105	Naturally flat smooth surface. Dry snow conditions
		B-η7%	4.5	73	7	118	51.2	3.6	105	5 Rectangular shapes
		B-η13%	4.5	63	13	129	45.5	3.6	105	10 Rectangular shapes
		B-η27%	4.5	49	27	142	40.0	3.6	105	20 Rectangular shapes
		B-smooth-wet	4.5	-	-	159	36.4	3.2	96.0	Naturally flat and smooth surface. Wet snow conditions
Arcelle (January-February 2019)	**C**	C smooth	86.0 – 100	-	0	137 – 211	66.1 – 78.9	3.3	169	Naturally flat smooth surface.
		C rough 90°	86.0 – 100	48.5 – 121	63	139 –211	66.9 – 78.1	3.3	166	20 Triangular shapes oriented at $\varphi_r = 90°$
		C rough 0°	86.0 – 100	-21.0 – 21.0	63	159 – 199	67.2 – 69.6	4.0	150	20 Triangular shapes oriented at $\varphi_r = 0°$
	D	D smooth	4.8 - 8.9	-	0	132-177	55.3 - 68.5	1.8	246	Naturally flat smooth surface.
		D rough 90°	4.8 - 8.9	41.0 – 73.0	63	131-161	55.3 - 65.1	1.4	281	20 Triangular shapes oriented at $\varphi_r = 90°$

2.2 Spectral albedo measurements

    Spectral albedo, or more precisely the bi-hemispherical reflectance (Schaepman-Strub et al., 2006), is the ratio of the upwelling and the downwelling spectral irradiance. Snow spectral albedo measurements were acquired with the Solalb instrument, a manual version of the albedometer AutoSolexs described by Picard et al. (2016). Solalb is a hand-held instrument

160   using a single light collector with a near-cosine response and equipped with an inclinometer located at the end of a 3 m boom. The boom was rotated by the operator to successively acquire the downward and upward solar radiation with a horizontal sensor (± 0.1° accuracy). This operation usually takes up to a maximum time of 30 seconds. Variations of incident illumination caused by clouds between two acquisitions were also measured with a photodiode receiving ambient radiation. Only spectra with stable incident illumination within 1 % were selected. Spectra were acquired over the 400-1050 nm wavelength range

165   with an effective resolution of 3 nm. The height of the sensor impacts the measured roughness effects, by changing the footprint of the sensor (L'Hermitte et al., 2014). To study this sensitivity, albedo was measured with sensor heights of 45 cm, 55 cm and 65 cm, in experiments A and B (not shown). We found a weak influence on measured albedo (0.4 ± 0.5 % of differences between spectra), showing that this sensitivity was negligible given the type of roughness considered here, and the sensor's height. Therefore, the sensor was set to 65 cm high for all experiments. At this height, the footprint is about 2.3 x 2.3 m² (99

170   % of the signal is coming from a viewing angle of 60°, Picard et al., 2016). The ratio of diffuse-to-total irradiance ($r_{diff\text{-}tot}$) was also measured shortly after the albedo measurement by screening the sun to record the diffuse irradiance, the total irradiance being measured with the sensor looking upward.

Post-processing was applied to each acquired spectrum following Picard et al. (2016). This includes dark current correction, considering the integration time, and the correction of the collector angular responses. The observed apparent albedo, called

175 α_{obs}, is the processed spectrum measured with Solalb, considering the sensor in a horizontal position (Sicart et al., 2001). The accuracy of α_{obs} mainly depends on that of the levelling of the arm. To estimate α_{obs} uncertainties, measurements were duplicated three times for 6 different sites. A maximal variation of 1.6 % was estimated between the α_{obs} spectra acquired in same field conditions.

2.3 Snow surface properties

180 Snow SSA was measured at the surface using the Alpine Snowpack Specific Surface Area Profiler (ASSSAP) instrument that has an accuracy of 10 % (Arnaud et al., 2011). For the two experiments A and B, only one surface SSA was measured, in the middle of the experiment (corresponding to $\eta = 13\%$), and the SSA was assumed to be constant throughout the experiments (3 hours). The albedo sensitivity to SSA variations and associated uncertainties is discussed in Sect. 4.2 in order to untwine these contributions from those of roughness. For the two experiments C and D, SSA were measured at the surface at each

185 albedo acquisition.

Moreover, albedo are highly impacted by the surface slope because of the change in the local incident solar angle (Grenfell et al., 1994). It has been shown that a slope of 2° facing the sun induces a variation in albedo by up to 5 % over a smooth surface (Dumont et al., 2017). An inclinometer fixed at the end of a 2 meter ruler was used to measure the slope in the sensor's footprint. The aspect of the slope is defined as the azimuth of the direction of the steepest slope, clockwise in degrees from

190 North. However, as the studied surfaces were chosen as flat as possible, the steepest inclination was not visually detectable. Thus, a first inclination measurement was acquired with the ruler parallel to the roughness features, and a second one by rotating the ruler by 90°, in order to estimate the normal of the surface ($\vec{n} = (n_x, n_y, n_z)$). The slope and the aspect were deduced as follow:

$$\theta_n = arccos(n_z) \qquad\qquad\qquad\qquad [1],$$

195 $$\varphi_n = - arctan(n_y/n_x) + \pi/2 \qquad\qquad\qquad\qquad [2],$$

where θ_n is the steepest slope angle, and φ_n is the aspect of the slope. In this study, all surface slopes were below 5°. The uncertainty of slope measurements was estimated of $\pm 1°$ due to natural ripples of the studied surfaces. The impact of this uncertainty in our roughness analysis is discussed in Sect. 4.2.

To limit the scope of this study, snow LAPs were not measured although they strongly lower the spectral signature in the

200 visible range, especially at the end of the season when the concentration of impurities is high at the surface (Flanner et al., 2009). It was the case for experiments A and B (measurements acquired in April). Figure 3 shows the spectrum measured over the A-smooth surface. The albedo decrease in the 400-600 nm range is a clear signature of a high LAP concentration. This sensitivity is well described in Dumont et al. (2017) and is out of the scope of this paper. However, to minimize this contribution, we chose to quantify effects of roughness in the 600-1050 nm wavelength range. Statistical results are given at

205 700 nm and at 1000 nm, to represent the visible and the NIR domain, respectively.
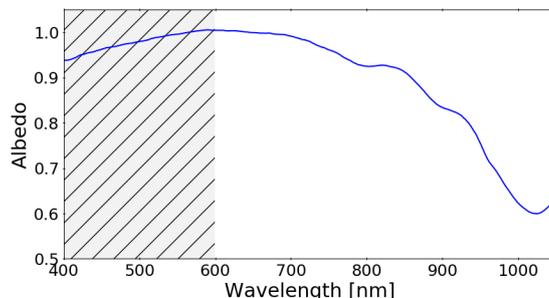
Figure 3. Measured spectral albedo from 400 nm to 1050 nm. The grey area with vertical lines (from 400 nm to 600 nm) is the wavelength range the most affected by the concentration of snow LAP (impurities). The spectrum is the one acquired over the A-smooth site (Table 1).

3 A 3-D Monte Carlo radiative transfer Model

The RSRT model was developed to simulate snow albedo considering macroscopic surface roughness. This combines both 1) the asymptotic radiative transfer theory (Sect. 3.1) to compute the spectral albedo each time a photon hits the modeled surface and 2) a Monte Carlo technique (Sect. 3.2) to estimate the geometric effects introduced by roughness and represented with a 3-D mesh of the studied area. Section 3.3 details the simulation framework and the sensitivity analysis. A simple approach is applied to estimate the impact of roughness on the quantity of energy absorbed in the snowpack (Sect. 3.4).

3.1 Asymptotic radiative transfer theory

In the RSRT algorithm, an ensemble of photons is launched over a modeled surface. This surface is represented with a triangular mesh composed of small facets. Both the spectral albedo and the BRDF distribution are computed for each facet hit by a photon. The Asymptotic Radiative Transfer theory (ART) provides analytical equations to estimate spectral albedo for highly reflective materials, which applies well to snow in the visible and the NIR domains, typically from 400 nm to 1100 nm (Zege et al., 1991; Kokhanovsky and Zege, 2004). Several models use this theory (Negi et al., 2011; Libois et al., 2013; Wang et al., 2017), which is based on three assumptions: 1) the snowpack is represented with vertically and horizontally homogeneous plane-parallel layers, 2) the surface is perfectly smooth and horizontal (flat), 3) single scattering albedo and the snow phase function are described with the asymmetry factor, g, the absorption enhancement parameter, B, and the SSA of the snow. The albedo simulated with the ART theory have shown a good accuracy compared to observations over smooth surfaces (Dumont et al., 2017; Wang et al., 2017). The facets of the mesh are small enough to be considered as smooth surfaces. The direct and the diffuse part of the albedo at the wavelength λ and θ_s, $\alpha_{dir}(\lambda, \theta_s)$ and $\alpha_{diff}(\lambda)$, are estimated with Eq. (3) and (4):

$$\alpha_{diff}(\lambda) = exp(-4\sqrt{\frac{2B\gamma(\lambda)}{3\rho_{ice}SSA(1-g)}}) \qquad [3],$$

$$\alpha_{dir}(\lambda, \theta_s) = exp(\frac{-12(1+2cos\theta_s)}{7}\sqrt{\frac{2B\gamma(\lambda)}{3\rho_{ice}SSA(1-g)}}) \qquad [4],$$

where B and g are assumed to be constant (B = 1.6 and g = 0.86, Libois et al., 2014b), ρ_{ice} = 917 kg m^{-3} is the bulk density of ice at 0°C, and $\gamma(\lambda)$ is the wavelength-dependent absorption coefficient of ice, taken from Picard et al. (2016) here.

The albedo of a flat smooth surface obtained with ART (α_{flat}) at wavelength λ and at θ_s is deduced as follows:

$$\alpha_{flat}(\lambda, \theta_s) = r_{diff-tot}(\lambda, \theta_s)\alpha_{diff}(\lambda) + (1 - r_{diff-tot}(\lambda, \theta_s))\alpha_{dir}(\lambda, \theta_s) \qquad [5],$$

where $r_{diff-tot}(\lambda, \theta_s)$ is the ratio of diffuse-to-total illumination at wavelength λ and at θ_s.

These formulations apply to a strictly leveled terrain (better than 0.5°). In the case of a tilted surface, the apparent albedo acquired with a sensor placed horizontally is different from α_{flat} because the surface receives sun radiation with a different

incidence angle and is viewed with a reduced solid angle by the sensor. To account for the slope and compute the apparent albedo of a titled smooth surface, called $\alpha_{sim,smooth}$, a K factor is applied (Dumont et al., 2017), such as:

$$K = cos(\theta_n) + tan(\theta_s)sin(\theta_n)cos(\varphi_s - \varphi_n) \qquad [6],$$

240   and:

$$\alpha_{sim,smooth}(\lambda, \theta_s) = r_{diff-tot}(\lambda, \theta_s).\alpha_{diff}(\lambda) + (1 - r_{diff-tot}(\lambda, \theta_s))K\alpha_{dir}(\lambda, \tilde{\theta}_s) \qquad [7],$$

where $\tilde{\theta}_s$ is the effective θ_s modified with the slope.

Following the ART theory, Kokhanovsky and Zege (2004) (further referred as the KZ04 approximations) estimated the snow BRDF distribution by calculating reflectance over a hemisphere with the reflection function of a semi-infinite medium:

245    $$R(\Phi, cos\theta_s, cos\theta_v) = R_0(\Phi, cos\theta_s, cos\theta_v) exp(\frac{-Ak_vk_s}{R_0}) \qquad [8],$$

where the function $R_0(\Phi, cos\theta_s, cos\theta_v)$ is the reflection function at $\omega_0 = 1$ (Kokhanovsky, 2013), with ω_0 the single scattering albedo. Φ is the relative azimuth angle, $cos\theta_v$ is the cosine of the viewing zenith angle, $cos\theta_s$ is the cosine of the solar zenith angle, and A is estimated as follows:

$$A = 4\sqrt{\frac{1-\omega_0}{3(1-g)}} \qquad [9].$$

250   k_s and k_v are called the escape functions, and are given by Kokhanovsky (2003) as:

$$k_s = \frac{3}{7}(1 + 2cos\theta_s) \qquad [10],$$

and:

$$k_v = \frac{3}{7}(1 + 2cos\theta_v) \qquad [11]..$$

3.2 Algorithms and model architecture

255   The Monte Carlo photon light transport algorithm propagates a large number of photons from their source to termination (i.e. escape from the scene). This algorithm is described in detail in the following.

A photon is a particle of light carrying a flux and described by its power (intensity), its origin $\vec{r}$, and its propagation direction $\vec{\iota}$. Each photon starts its trajectory with an intensity equal to 1 (unitless quantity of energy), and a direction $\vec{\iota}$ described with the couple (θ_s, φ_s) given as input. Photons are either absorbed or reflected at each hit according to the facet albedo (Iwabuchi,

260   2006). A flow chart of a photon path as computed with RSRT is presented in Figure 4. This is computed in four main steps.

Step 1: Estimate the next intersection of the photon with the mesh of the surface (called "hit"). The Bounding Volume Hierarchies (BVH) technique (Ize, 2013) is used to efficiently search for the first facet in the photon propagation direction. The precise intersection point within the facet is determined by applying the watertight ray/triangle intersection algorithm (Woop et al., 2013). If the photon hits a facet, its origin $\vec{r}$ is updated on the intersected facet. The normal of the facet is

265   estimated. If there is no hit, the photon escapes from the mesh, and depending on its direction (upward or downward), its intensity is added to the down or up welling radiation bin (Fig. 4).

Step 2: Update the intensity. The photon intensity at hit n (called $i_{p,n}$) is weighted by the spectral albedo accounting for the incoming direction angles $\alpha_{flat}(\lambda, \theta_i)$ as follows:

$$i_{p,n+1} = i_{p,n}\alpha_{flat}(\lambda, \theta_i) \qquad [12],$$

270   Two configurations are possible (Sect. 3.3). With the KZ04 configuration, the hit facet is considered as a snow surface and $\alpha_{flat}(\lambda, \theta_i)$ is estimated by considering the local incident angle θ_i and snow properties (SSA, B, g) (i.e. with ART, Eq. (5)). With the Lambertian configuration, the hit facet is a Lambertian surface (i.e. isotropic diffusion), and the $\alpha_{flat}(\lambda, \theta_i)$ is a constant value equal to $\alpha_{flat}(\lambda)$, given as input.

Step 3: Sample the outgoing direction. The most likely outgoing direction of the photon after a hit is estimated from the

275   BRDF distribution computed with the KZ04 approximations (Sect. 3.1). BRDF values are estimated for all directions, defined

by the ($\cos\theta_v$, φ_v) couples. The outgoing direction is sampled from the BRDF distribution using a rejection algorithm as follows: in a first step, the azimuth φ_v is sampled from a uniform distribution between 0 and 2π, and $\cos\theta_v$ with a uniform distribution between 0 and 1, so that the hemisphere is sampled with a cosine weighting distribution (Greenwood, 2002). In a second step, a probability of acceptance is given to each direction (θ_v, φ_v). This probability of acceptance is estimated by the BRDF value
280 in this direction, normalized by the maximum value of the BRDF distribution.

Step 4: Update the direction $\vec{\iota}$. The new photon direction $\vec{\iota}_{n+1}$ after the hit n is updated as follows:

$$\vec{\iota}_{x,n+1} = \vec{\iota}_n - \cos\theta_i . \vec{n} \qquad\qquad [13],$$

$$\vec{\iota}_{y,n+1} = \vec{n} \times \vec{\iota}_{x,n} \qquad\qquad [14],$$

$$\vec{\iota}_{n+1} = \sin\theta_i\,(\vec{\iota}_{x,n+1}.\cos\varphi + \vec{\iota}_{y,n+1}.\sin\varphi) - (\vec{\iota}_n.\vec{n}).\vec{n} \qquad\qquad [15],$$

285 With $\vec{\iota}_{x,n}$ and $\vec{\iota}_{y,n}$ the photon directions in the x and y axis before the hit n, respectively.

The algorithm returns to step 1 until the photon escapes from the scene (Fig. 4), or until its intensity is lower than a threshold (set to 0.01 in RSRT). To ensure an unbiased termination in the latter case, a 'Russian roulette' method is applied (Iwabuchi, 2006), which consists in: accepting or rejecting the termination with probabilities $1-p$ and p, respectively ($p = 0.2$ in RSRT). In case of rejection, the weak intensity of the photon is rescaled by the factor $1/p$, and the algorithm goes again to step 1. As
290 explained by Iwabuchi (2006), the total energy is conserved for any p value, and this approach can be applied at any step of the algorithm.

At the end of its path, the photon intensity is counted in: 1) the total upward intensity ($I_\uparrow$) if the photon escapes with an upward direction, 2) the intensity lost downward if its final z axis direction is downward (this is possible with a tilted surface for instance). If the latter contribution is higher than 10^{-3} for a horizontal rough surface, we consider that too many photons
295 have been lost to output a realistic albedo, meaning that the simulation used a too wide radiation source or conversely a too small mesh area.
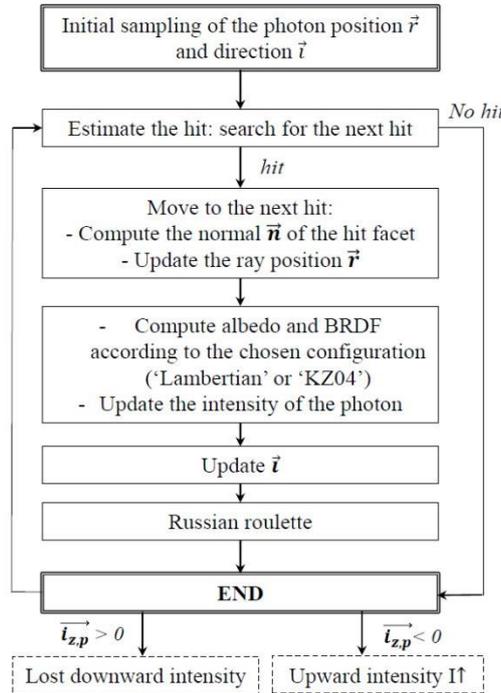
Figure 4. Flow chart of a photon path in the RSRT algorithm. $\vec{\iota}$ is the incident direction of the photon, $\vec{\iota}_{z,p}$ is the z axis component of the photon at the end of its path.

3.3 Simulation framework

3.3.1 Model simulations

RSRT is run here either by considering the snow surface 1) as Lambertian (Lambertian configuration), the albedo is not sensitive to the incident angle and each photon hitting the mesh is reflected with a constant facet albedo equal to $\alpha_{flat}(\lambda)$, or 2) as a snow surface using KZ04 analytical equations (referred to as the KZ04 configuration). In this latter configuration, each photon hitting the mesh is reflected with $\alpha_{flat}(\lambda, \theta_i)$, which depends on the incident angle θ_i, SSA, B and g values, i.e. by considering the intrinsic BRDF of the snow. The two configurations are compared in Sect. 4.3. The KZ04 configuration is used by default in for all other simulations to compare with observations.

RSRT inputs are described in Table 2. Triangular meshes of rough surfaces are modelled by reproducing same linear shapes as those created in the field with an orientation φ_r, a height H, a width W, and spaced by a constant distance defined with the period Λ (as shown in Figure 1, with same values as in Table 1). Meshes have a spatial resolution of 1 cm and are produced large enough to be considered as infinite (no edge effects). When a RSRT simulation is started, an ensemble of photons is first created on a horizontal plane above the surface mesh and distributed quasi-randomly to produce a parallel source. The size of the photon ensemble is set to 10^6 photons as a compromise between the computing time and a good representation of the emission source. The direction of propagation of the ensemble of photon is initialized with the solar zenith and azimuth angles given as inputs.

RSRT outputs the snow spectral albedo, either in direct or diffuse illumination conditions: $\alpha_{dir,rough}(\lambda, \theta_s)$ and $\alpha_{diff,rough}(\lambda)$, respectively, considering that the plane of the mesh is perfectly flat. To take into account the slope, $\alpha_{dir,rough}(\lambda, \theta_s)$ and $\alpha_{diff,rough}(\lambda)$ are combined with Eqs. (6) and (7) to simulate the apparent snow albedo of a titled rough surface, called $\alpha_{sim,rough}(\lambda, \theta_s)$.

Table 2. RSRT inputs description

Inputs	Description	Units	Lambertian	KZ04
ϑ_s	Zenith angle of the radiation source	Degrees (clockwise)	x	x
φ_s	Azimuth angle of the radiation source	Degrees (clockwise, 0° is North)	x	x
Mesh	Triangular mesh	With a 1 cm spatial resolution	x	x
z scale	Additional scaling coefficient of the mesh in the z axis. 1 is default, 0 to simulate a flat smooth surface	No units	x	x
$N_{photons}$	Size of the photon ensemble	No units	x	x
φ_r	Azimuthal orientation of the mesh around the z axis	Degrees (clockwise, 0° is North)	x	x
Facet albedo	Constant albedo $\alpha_{flat}(\lambda)$	No units. By default = 0.8	x	
B, g	Snow shape coefficients (Libois et al., 2014b)	No units		x
SSA	Specific Surface Area of snow	$m^2 kg^{-1}$		x

3.3.2 Evaluation of simulations

The evaluation of simulations was treated over a set of N observations using the Root Mean Square Deviation (RMSD), defined as follow:

$$RMSD(\lambda, \theta_s) = \sqrt{\frac{\sum_{i=1}^{N}(\alpha_{sim,i}(\lambda,\theta_s) - \alpha_{obs,i}(\lambda,\theta_s))}{N}} \qquad [16]$$

with $\alpha_{sim,i}(\lambda, \theta_s)$ the ith simulation (either $\alpha_{sim,smooth}$ or $\alpha_{sim,rough}$) at the wavelength λ and θ_s, and $\alpha_{obs,i}(\lambda, \theta_s)$ the ith measured albedo. The performances of $\alpha_{sim,smooth}(\lambda, \theta_s)$ and $\alpha_{sim,rough}(\lambda, \theta_s)$ are compared to evaluate the accuracy gain acquired by taking into account surface roughness. We further called $\overline{RMSD}$, the RMSD(λ, θ_s) averaged over the 600-1050 nm range for one spectra.

3.3.3 Impact of uncertainties

Albedo observations may have been affected by uncertainties or unmeasured variations. To investigate the potential impact,

330 we conducted the following simulations. Firstly, SSA may have varied over time in experiments A and B, whereas albedo was simulated with a constant SSA. In order to estimate these variations, we retrieved SSA at the beginning of the experiments from albedo observations over the smooth surfaces, by fitting $\alpha_{sim,smooth}$ with α_{obs} using the same approach as described by Libois et al. (2015). RSRT was then run by considering retrieved SSA (SSA$_r$) for simulations over A-smooth and B-smooth-dry surfaces, and the measured SSA (SSA$_m$) for simulations over the rough surfaces. Results are studied at 1000 nm where the

335 sensitivity to SSA is larger (Dominé et al., 2006). Secondly, the difference between retrieved and measured SSA may be related to the uncertainty in SSA measurements. We explored the impact of SSA uncertainties with RSRT simulations by varying SSA$_m$ by ± 10 % over the rough surfaces at 1000 nm. Thirdly, the impact of slope uncertainties was studied with RSRT simulations by varying the slope of the rough surfaces by ± 1° in experiments C rough 90° and D rough 90° at 1000 nm. We used C and D experiments only since observations over the rough and smooth surfaces were acquired simultaneously, with similar θ_s values (to not influence $\widetilde{\theta_s}$ the effective θ_s modified with the slope).

340 similar θ_s values (to not influence $\widetilde{\theta_s}$ the effective θ_s modified with the slope).

3.3.4 Analysis of processes introduced by surface roughness

The variations of illumination conditions and SSA may attenuate or accentuate roughness effects by playing a role either in the effective angle effect, or in multiple reflections. We thus investigated separately these effects as a function of illumination conditions and SSA to better characterize roughness effects.

345 The effective angle effect is the alteration of the local incident angle over roughness shapes. It was simulated with RSRT using the KZ04 configuration (albedo varying with θ_s) and by requiring that photons hit the surface only once, i.e. without multiple reflections. The total upward and downward intensities were then added to count all the photons that have not been absorbed after the first hit. We also conducted same simulations with the Lambertian configuration to check there was no angular dependence. These simulations were performed with various illumination conditions.

350 The effect of multiple reflections caused by the photon trapping depends on the albedo value. While the effective angle effect is significant under direct sunlight only, this second effect is significant both under direct and diffuse illumination (Warren et al., 1998). Therefore, it was simulated by running RSRT under diffuse sunlight. Simulations were conducted for various SSA.

4 Results and discussion

We explore the albedo sensitivity to macroscopic surface roughness through three questions: 1) is it possible to quantify the

355 change in albedo caused by surface roughness, and to model this contribution (Sect. 4.1)? 2) What is the impact of SSA and slope uncertainties in the quantification of roughness effects (Sect. 4.2.)? 3) What are the respective roles of the effective angle effect and multiple reflections according to snow properties and illumination conditions (Sect. 4.3)? The impact of roughness on the absorbed energy is also investigated (Sect. 4.4).

4.1 Albedo sensitivity to roughness features

4.1.1 Sensitivity to the fraction of roughness features

360

Figure 5 shows measured and simulated spectral albedo between 600-1050 nm for experiment A (Sect. 2.1). From Fig. 5a to Fig. 5d, α_{obs} decreases while the fraction of roughness features (η = W/Λ) increases. Indeed, while the number of roughness shapes increases, more photons are trapped between concavities. They have a larger probability to be absorbed (one probability

at each hit) relative to a smooth surface (only one hit), causing the observed albedo decrease. Note that the pattern of the

365 measured spectra between 600-700 nm is probably led by a high concentration of snow LAPs (not visible to the naked eye on the field).

By neglecting the presence of roughness, $\alpha_{sim,smooth}$ spectra increase due to larger θ_s from A-smooth to A-η27% (the sun went down). Indeed, photons penetrate less deeply into the snowpack as they enter with a grazing angle (large θ_s). They encounter the first scattering event near the surface and has more probability to escape compared to a photon penetrating deeper with a

370 low θ_s (Carroll and Fitch, 1981; Warren, 1982). The bias between α_{obs} and $\alpha_{sim,smooth}$ becomes higher while η increases ($\overline{RMSD}$= 0.06 when η = 27%). On the contrary, by considering the presence of roughness, $\alpha_{sim,rough}$ spectra follow the observed trend, and decrease while η increases (even if θ_s becomes larger). *Simulations are strongly improved compared to $\alpha_{sim,smooth}$ that neglects surface roughness ($\overline{RMSD}$= 0.02 when η = 27%). Nevertheless, reductions in albedo are not clearly quantifiable from one rough surface to another (from A-η7% to A-η13%, for instance). Results are thus further plotted at two wavelengths only,

375 700 nm and 1000 nm.*
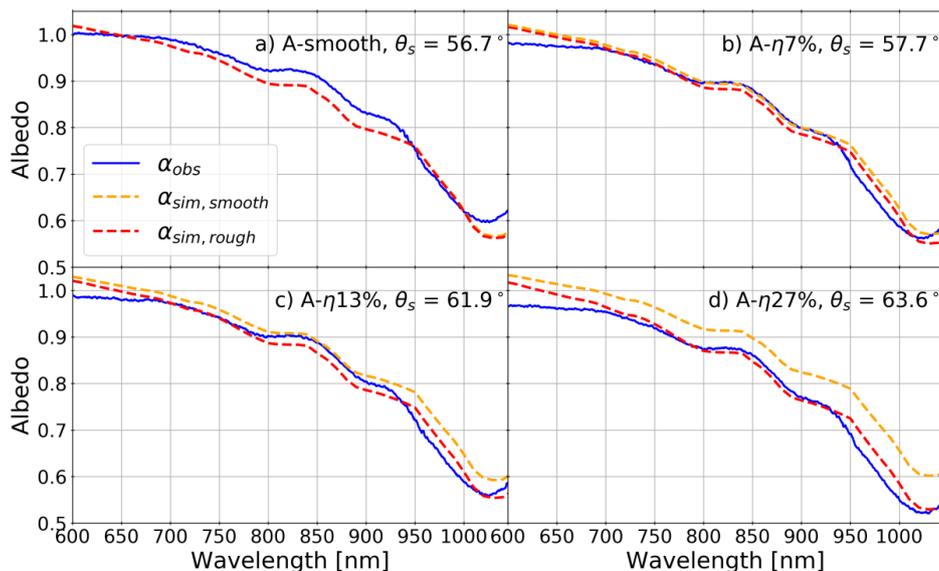
Figure 5. Measured spectral albedo α_{obs} (blue full lines), and simulated spectral albedo considering a smooth surface with the ART theory ($\alpha_{sim,smooth}$, orange dotted lines), and a rough surface with RSRT ($\alpha_{sim,rough}$, red dotted lines) for the surfaces a) A-smooth, b) A-η7%, c) A-η13%, and d) A-η27%.

380

To highlight the roughness effect, Figure 6 shows the change in albedo with increasing roughness fraction η relative to the initial smooth surface, for both observations and simulations of experiments A and B, i.e. $\Delta\alpha_{obs}(\lambda, \theta_s) = \alpha_{obs}(\lambda, \theta_s) - \alpha_{obs}(\lambda, \theta_{s,o})$ and $\Delta\alpha_{sim,rough}(\lambda, \theta_s) = \alpha_{sim,rough}(\lambda, \theta_s) - \alpha_{sim,smooth}(\lambda, \theta_{s,o})$. However, this change in albedo is also affected by concomitant changes of the solar zenith angle, as roughness features were added progressively to the initially smooth surface (Fig. 2). To quantifiy

385 the impact of this spurious change, Fig. 6 also shows the simulated change in albedo if the surface had remained smooth ($\Delta\alpha_{sim,smooth}(\lambda, \theta_s) = \alpha_{sim,smooth}(\lambda, \theta_s) - \alpha_{sim,smooth}(\lambda, \theta_{s,o})$).

In experiment A, the stronger $\Delta\alpha_{obs}$ decrease is of 0.03 at 700 nm, and of 0.07 at 1000 nm, between A-η27% (η = 27 %, θ_s = 63.6°) and A-smooth *(η = 0 %, $\theta_{s,0}$ = 56.7°)* (Fig. 6a and 6c). Experiment A-η7% shows that even a low fraction of roughness features causes an albedo decrease of 0.02 (0.03) compared to that of a smooth surface at 700 nm (1000 nm). $\Delta\alpha_{obs}$ decreases

390 whereas θ_s increases, showing that albedo is more sensitive to roughness effects than to θ_s variations here. This result highlights the need to consider the presence of roughness in albedo simulations.

While θ_s becomes larger, $\Delta\alpha_{sim,smooth}$ increases by 0.02 at 700 nm, and by 0.03 at 1000 nm, between A-$\eta27\%$ and A-smooth (Fig. 6a and 6c). By considering roughness in simulations, $\Delta\alpha_{sim,rough}$ decreases by 0.01 at 700 nm, and by 0.03 at 1000 nm between A-$\eta27\%$ and A-smooth. Simulations are thus improved by accounting for surface roughness but RSRT (i.e. $\alpha_{sim,rough}$)

395 underestimates by almost a factor 2 the observed albedo reduction.

In experiment B, $\Delta\alpha_{obs}$ shows a strong decrease of 0.11 at 700 nm, and 0.15 at 1000 nm, between B-$\eta27\%$ ($\eta = 27$ %, $\theta_s =$ 39.9°) and B-smooth-dry ($\eta = 0$ %, $\theta_s = 55.4°$) (Fig. 6b and 6d). In this experiment, α_{obs} decreases due both to the θ_s decrease (the sun went up, Sect. 2.1) and the η increase. To remove θ_s contribution, we use the $\Delta\alpha_{sim,smooth}$ trend that depends on θ_s variations only: $\Delta\alpha_{sim,smooth}$ lowers when θ_s decreases and the reduction is half of that of $\Delta\alpha_{obs}$ (0.05 at 700 nm, and 0.07 at 1000

400 nm when $\eta = 27\%$). Therefore, half of the α_{obs} decrease is attributable to the decrease in θ_s, and the other half to the presence of roughness.

$\Delta\alpha_{sim,rough}$ decreases by 0.07 at 700 nm, and 0.11 at 1000 nm, between B-$\eta27\%$ and B-smooth-dry (Fig. 6b and 6d). Simulations are more consistent with observations by considering the presence of roughness, but the simulated decrease is still underestimated compared to measurements, as for experiment A.

405 To accurately quantify roughness effects on albedo, it is important to compare rough and smooth surfaces for similar snow and illumination conditions. This is why we simultaneously measured albedo over B-$\eta27\%$ ($\eta = 27$ %, $\theta_s = 39.9°$) and a nearby smooth surface (the B-smooth-wet surface: $\eta = 0\%$, $\theta_s = 36.4°$, Table 1 and Fig. 6b and 6d). The concurrent measurements show a decrease by 0.05 at 700 nm, and 0.07 at 1000 nm. This reduction is solely attributable to the presence of roughness. It is similar to the $\Delta\alpha_{obs}$ decrease by subtracting the $\Delta\alpha_{sim,smooth}$ that is caused by the θ_s decrease only (Fig. 6).

410 For both experiments, observations show that the albedo decrease is stronger when 1) the number of roughness features is larger, and 2) at the longer wavelengths. As albedo is lower in the NIR domain, the impact of multiple reflections is stronger. Indeed, the effect of multiple reflection is more important for intermediate values than for albedo close to 0 or 1 (i.e. systematic absorption or reflection, Warren et al., 1998).

Table 3 shows that RMSDs estimated for $\alpha_{sim,smooth}$ increase with the fraction of roughness features, and are higher at 1000

415 nm than at 700 nm. By considering roughness in the RSRT model, the accuracy of $\alpha_{sim,rough}$ is improved by about a factor 2 at 700 nm and 1000 nm compared to $\alpha_{sim,smooth}$ (average $\alpha_{sim,rough}$ RMSD of 0.02 at 700 nm and 1000 nm).
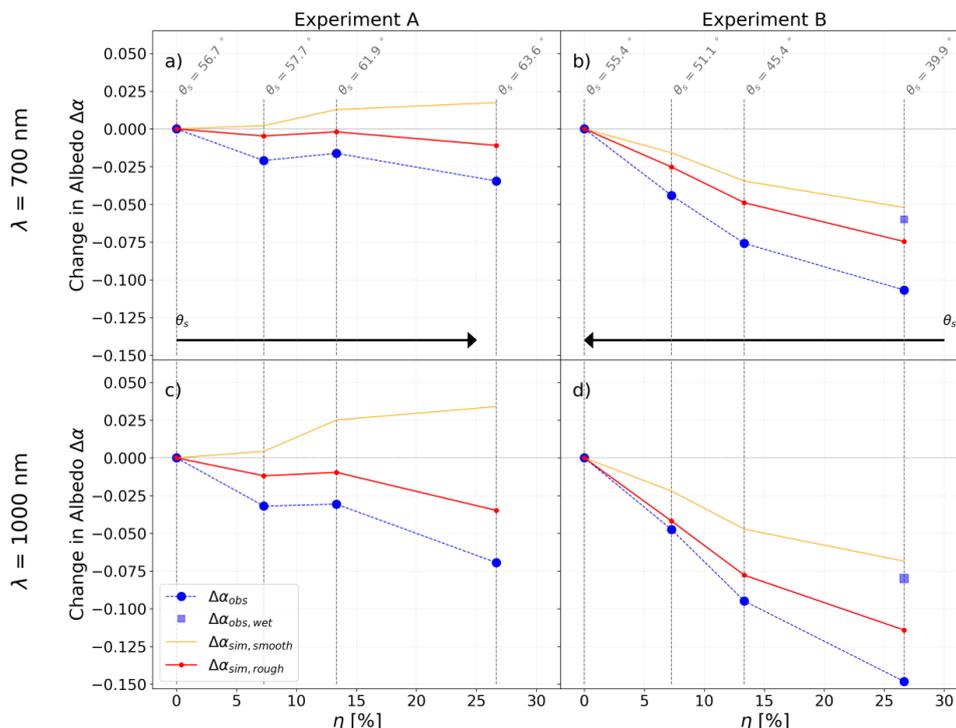
Figure 6. Variations of albedo differences between the albedo at θ_s and the albedo at $\theta_{s,o}$, corresponding to that of the smooth surface, as a function of the η ratio (W/Λ in %). Blue points are $\Delta\alpha_{obs}(\lambda, \theta_s)$ ($=\alpha_{obs}(\lambda, \theta_s) - \alpha_{obs}(\lambda, \theta_{s,o})$), orange lines are $\Delta\alpha_{sim,smooth}$ ($=\alpha_{sim,smooth}(\lambda,$
420 **$\theta_s) - \alpha_{sim,smooth}(\lambda, \theta_{s,o})$), where variations are due to θ_s changes only ($\eta=0\%$ for all simulations), and red lines are $\Delta\alpha_{sim,rough}$ ($=\alpha_{sim,rough}(\lambda,$ $\theta_s) - \alpha_{sim,smooth}(\lambda, \theta_{s,o})$), which varies with η and θ_s. Blue squares are the $\Delta\alpha_{obs,wet}(\lambda, \theta_s)$ ($=\alpha_{obs}(\lambda, \theta_s) - \alpha_{obs\text{-}wet}(\lambda, \theta_{s,0})$) where $\alpha_{obs,wet}$ is the measured albedo over the B-smooth-wet surface ($\eta=0\%$ and $\theta_s=39.9°$, Table 1). Grey vertical lines describe the solar zenith angle (θ_s) when measurements were acquired. Results are given for a) experiment A at 700 nm; b) Same as a) but for experiment B; c) experiment A at 1000 nm; d) Same as c) but for experiment B.**

425

Table 3. RMSD of $\alpha_{sim,smooth}$ and $\alpha_{sim,rough}$ at 700 nm and 1000 nm. RMSD is calculated with Eq. (16). N is the number of studied surfaces.

	η	$\lambda = 700$ nm		$\lambda = 1000$ nm	
		$\alpha_{sim,smooth}$	$\alpha_{sim,rough}$	$\alpha_{sim,smooth}$	$\alpha_{sim,rough}$
Experiments A and B (N=2)	7 %	0.02	0.01	0.03	0.01
	13 %	0.03	0.02	0.05	0.02
	27 %	0.04	0.02	0.09	0.03
Experiments C and D (N = 19)	63 %	0.07	0.03	0.09	0.04
Total (N = 21)	7-63 %	0.06	0.03	0.08	0.04

4.1.2 Sensitivity to the roughness orientation

In experiments C and D, albedo measurements are simultaneously acquired over a rough surface and a nearby smooth surface
430 for multiple illumination conditions, every 20 minutes. A spectral analysis of the impact of roughness is first discussed, using a randomly chosen illumination condition for each experiment. Then, the albedo sensitivity to the roughness orientation with respect to the solar azimuthal angle ($\Delta\varphi_r$) is investigated at two wavelengths.

- Spectral analysis:

Spectral albedo simulations are performed for experiments C at $\theta_s \sim 68°$ and D at $\theta_s \sim 59°$. Results are shown in Figure 7.

435 α_{obs} spectra show a significant decrease caused by the presence of surface roughness (~ -0.05 on average, Fig. 7a and 7d), more pronounced in the NIR domain. $\alpha_{sim,smooth}$ spectra are identical over the smooth and rough surfaces since illumination conditions are similar (dotted lines in Fig. 7 and 7e). For these illumination conditions, $\alpha_{sim,smooth}$ spectra over the rough surfaces show a strong deviation compared to α_{obs}, with a $\overline{RMSD}$ 0.04 and 0.05 for C rough 0° and C rough 90°, respectively, and of 0.06 for D rough 90°. By considering roughness, $\alpha_{sim,rough}$ spectra reproduce the observed decrease (~-0.05, Fig. 7c and 7f). Simulations

440 are improved compared to $\alpha_{sim,smooth}$, with a $\overline{RMSD}$ of 0.02 and 0.04 for C rough 0° and C rough 90°, and of 0.04° for D-rough90.
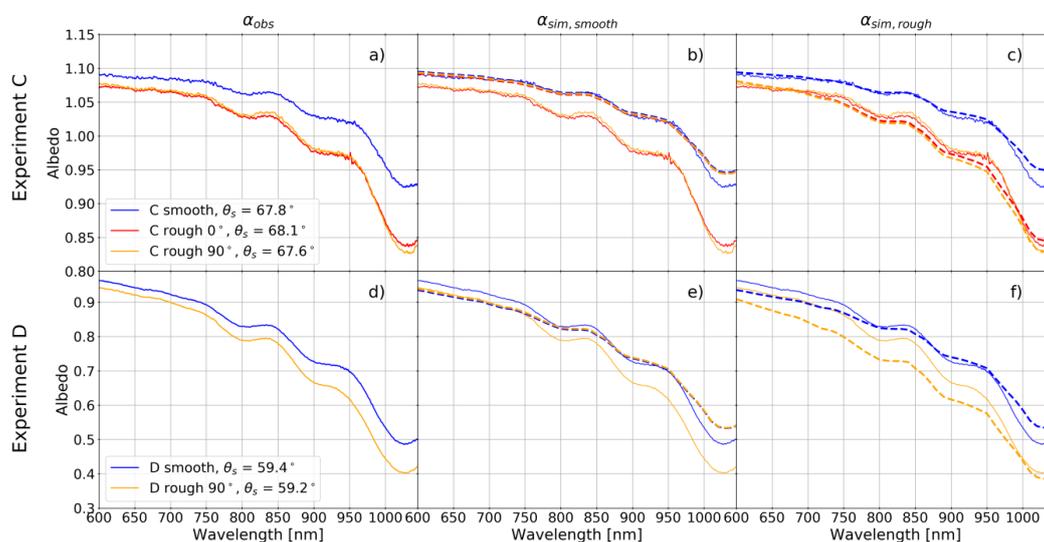
Figure 7. Spectral albedo variations for experiment C at $\theta_s \sim 68°$ with a) α_{obs}; b) α_{obs} (full lines) and $\alpha_{sim,smooth}$ (dotted lines), c) α_{obs} (full lines) and $\alpha_{sim,rough}$ (dotted lines). Red lines represent the C rough 0° surface, yellow lines the C rough 90° surface and blue lines the
445 **C smooth surface. Figures d), e) and f) are similar but for experiment D at $\theta_s \sim 59°$. Orange lines represent the D rough 0° surface and blue lines the D smooth surface.**

- Effects of roughness with varying illumination conditions:

Figure 8 shows the change in albedo as a function of $\Delta\varphi_r$ at 700 nm and 1000 nm. $\Delta\alpha_{obs}$ is the difference between α_{obs}

450 simultaneously acquired over the rough and the smooth surfaces. Similarly, $\Delta\alpha_{sim,rough}$ is the difference between $\alpha_{sim,rough}$ simulated over the rough surface and $\alpha_{sim,smooth}$ simulated over the smooth surface, at same illumination conditions. Thus, the change in albedo is not correlated to θ_s here, but to φ_s that leads the roughness orientation with respect to the sun position.

When roughness features are parallel to the sun (when $\Delta\varphi_r = 0°$ for C rough 0°, Fig. 8a and 8d), α_{obs} decreases of 0.01 at 700 nm, and of 0.08 at 1000 nm, relative to a smooth surface (Fig. 8a and 8d). The impact becomes larger when the roughness

455 orientation is perpendicular to the sun (when $\Delta\varphi_r = 90°$ for C rough 90°, Fig. 8b and 8e), with an α_{obs} decrease of 0.03 at 700 nm and of 0.10 at 1000 nm. For this case, the reduction in albedo is 20 % stronger when roughness features lie perpendicular to the sun than when they are parallel. When the sun elevation is low, if the roughness orientation is perpendicular to the sun, the effective incident angle over sides facing the sun is decreased compared to that of a smooth surface. In addition, the fraction of shadow is higher when $\Delta\varphi_r = 90°$. This effective angle effect leads to an average decrease in snow albedo relative to a

460 smooth surface. However, for the C rough 90° experiment, $\Delta\varphi_r$ varies from 50° to 122° and $\Delta\alpha_{obs}$ does not show a strongest albedo reduction around 90°. The SSA is particularly high for this experiment (~100 m^2 kg^{-1}) and it may explain the albedo insensitivity to weak variations of roughness orientation.

In experiment C, $\Delta\alpha_{sim,rough}$ variations reproduce well the $\Delta\alpha_{obs}$ decrease, with the same order of magnitude: the average decrease is of 0.01 at 700 nm and 0.08 at 1000 nm for C rough 0°, and of 0.02 at 700 nm and 0.10 at 1000 nm for C rough 90° (Fig. 8a and 8d).

In experiment D rough 90°, measurements were acquired in the morning, so $\Delta\varphi_r$ varies from 42° to 72° (Fig. 8c and 8f). We measured an average $\Delta\alpha_{obs}$ decrease of 0.02 at 700 nm and 0.09 at 1000 nm, which is in agreement with results found for C rough 90°. The observed pattern of $\Delta\alpha_{obs}$ shows oscillations, probably caused by differences in snow properties between the smooth and the rough surfaces. SSA was measured over the smooth surface to be representative, while SSA values over rough surfaces evolved with spatial variations according to the received illumination. In addition, for this experiment, melting was observed at the surface, resulting in a smoothing of our roughness shapes during the day. This is certainly why in Fig. 8c and 8f, the $\Delta\alpha_{obs}$ increases from 42° to 72°, while in theory it should decrease when $\Delta\varphi_r$ approaches 90°.

Fig. 8c and 8f shows that $\alpha_{sim,rough}$ overestimates by almost a factor 2 the reduction in α_{obs}: the average $\Delta\alpha_{sim,rough}$ decrease is of 0.06 at 700 nm, and of 0.15 at 1000 nm. By considering roughness shapes constant along the day, $\Delta\alpha_{sim,rough}$ decreases from 42° to 72° (i.e. $\Delta\varphi_r$ gets closer to 90°).

Considering all observations of experiments C and D, $\alpha_{sim,rough}$ is significantly improved compared to $\alpha_{sim,smooth}$, with an averaged RMSD of 0.03 at 700 nm and 0.04 at 1000 nm (against an averaged RMSD of 0.07 at 700 nm and 0.09 at 1000 nm for $\alpha_{sim,smooth}$, Table 2).

To sum up, observations show that an increase of the number of roughness features leads to a larger reduction in α_{obs}, with a higher sensitivity in the NIR domain. Roughness effects are also larger when the roughness orientation is perpendicular to the sun rather than parallel. The maximal α_{obs} decrease is of 0.03 at 700 nm, and 0.10 at 1000 nm, for C rough 90°. Considering all observations, $\alpha_{sim,rough}$ are improved by a factor 2 at 700 nm and 1000 nm compared to $\alpha_{sim,smooth}$, with an average RMSD of 0.03 at 700 nm and 0.04 at 1000 nm (Table 2). $\alpha_{sim,rough}$ shows an underestimation of the observed albedo decrease, but observations may have been affected by uncertainties or unmeasured variations.
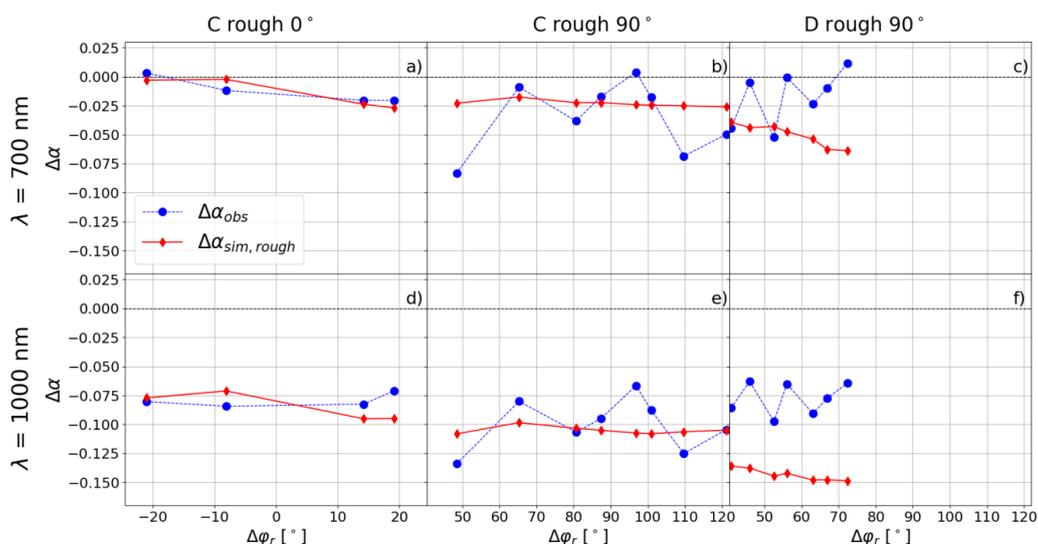
Figure 8. Measured and simulated variations of Δα (=[rough-smooth] at the same θ_s) at 700 nm as a function of $\Delta\varphi_r$ for a) the C rough 0° experiment, b) the C rough 90° experiment, c) the D rough 90° experiment. d), e) and f) are the same but at 1000 nm. Blue points are $\Delta\alpha_{obs}$, and red lines with diamonds are $\Delta\alpha_{sim,rough}$. The horizontal black dotted lines are the reference showing the 0.

4.2 Analysis of uncertainties

In a first step, we explore the possible SSA variations in experiments A and B, and the impact on snow albedo. In a second step, we integrate SSA and slope uncertainties in our roughness analysis.

4.2.1 Sensitivity to SSA

495   By fitting $\alpha_{sim,smooth}$ and α_{obs} over the smooth surface (Sect. 3.3), we estimate an SSA (written SSA$_r$) of 9.4 m^2 kg^{-1} over A-smooth and 5.3 m^2 kg^{-1} over B-smooth. Measured SSA (SSA$_m$) are equal to 7.4 m^2 kg^{-1} over A-$\eta 13\%$ and 4.5 m^2 kg^{-1} over B-$\eta 13\%$. Hence, for both experiments, there is a decrease in SSA from the beginning (smooth surface, $\eta = 0\%$) to $\eta = 13\%$, which is compatible with the observation of melt at the surface during these two experiments performed in April. Grenfell and Maykut (1977) explained that snow albedo decreases when liquid water replaces air between ice grains. The refractive index of the

500   water being very close to that of ice, this results in an increases the effective grain size.

To explore the impact of a decreasing SSA on albedo, RSRT is run by considering SSA$_r$ for simulations over A-smooth and B-smooth-dry surfaces (SSA$_r$ equal to 9.4 m^2 kg^{-1} and 5.3 m^2 kg^{-1}, respectively), and SSA$_m$ for simulations over the rough surfaces (from $\eta = 7\%$ to 27%, SSA$_m$ equal to 7.4 m^2 kg^{-1} and 4.5 m^2 kg^{-1}, Table 1). Results are presented in Figure 9, where $\Delta\alpha_{sim,rough,ssa}$ is the difference $\alpha_{sim,rough}(\lambda, \theta_s, SSA_m) - \alpha_{sim,smooth}(\lambda, \theta_{s,o}, SSA_r)$. Compared to $\Delta\alpha_{sim,rough}$ (i.e. constant SSA), the $\Delta\alpha_{sim,rough,ssa}$

505   decrease is multiplied by a factor two by considering both the increase in the fraction of roughness features, and the SSA decline from 9.4 to 7.4 m^2 kg^{-1} (-15 %) for experiment A, or from 5.3 to 4.5 m^2 kg^{-1} (-21 %) for experiment B (Fig. 9a and 9b). $\Delta\alpha_{sim,rough,ssa}$ reproduces well the $\Delta\alpha_{obs}$ decrease, with the same order of magnitude. Therefore, both SSA variations and roughness effects overlap and lower snow albedo in these two experiments, making it difficult to accurately isolate roughness effects.

510   Differences between retrieved and measured SSA may be explained by the uncertainty in SSA measurements. The impact of SSA uncertainties is investigated by varying SSA by $\pm 10\%$ in RSRT simulations. Obtained values range within the grey shade shown in Figure 9. Experiment C has a large SSA (~ 100 m^2 kg^{-1}), typical of fresh fallen snow, and SSA uncertainties weakly affect $\Delta\alpha_{sim,rough}$ (Fig. 10c). On the contrary, a variation of $\pm 10\%$ in SSA strongly impacts the experiments with a low SSA: $\Delta\alpha_{sim,rough,ssa}$ varies between 0.05-0.10 in experiment A-$\eta 27\%$ (Fig. 9a), between 0.11-0.16 in experiment B-$\eta 27\%$ (Fig. 9b),

515   and between 0.13-0.18 in experiment D when $\Delta\varphi_r = 72°$ (Fig. 9d). The reduction in albedo is stronger when SSA is lower due to higher absorption. More precisely, the grains at the surface control the first scattering event and large-coarse grains (i.e. low SSA) are both more absorptive and more forward scattering relative to fine grains since photons have to pass through longer paths in ice before being potentially scattered at the ice-air interfaces (Warren et al., 1998). Dominé et al. (2006) have shown that the SSA-albedo relationship is non-linear and that albedo varies weakly in the NIR domain when SSA > 30 m^2 kg^{-1}, while

520   it is highly sensitive to SSA variations for SSA values below 10 m^2 kg^{-1}. Hence, while a large SSA leads to a weaker impact of multiple reflections (high albedo), the impact of the photon trapping is more important at low SSA (<10 m^2 kg^{-1}).

Experiment D highlights that the impact of SSA uncertainties in albedo is linked to the roughness orientation (Fig. 9d). Albedo is twice as sensitive to SSA when $\Delta\varphi_r = 72°$ as when $\Delta\varphi_r = 42°$. This is caused by the effective angle effect introduced by roughness: photons penetrate deeper over sides facing the sun when the roughness orientation is perpendicular to the sun (lower

525   incident angle) than if it was oblique or parallel. When SSA is low, absorptions increase and a photon has larger probability to be absorbed by penetrating deeply in the snowpack. Hence, the effective angle effect is more pronounced when roughness orientation is perpendicular to the sun and for low SSA.

The joint impact of roughness effects and SSA in the NIR domain has consequences on the accuracy of SSA retrievals. Several

530   studies directly used the ART equations to retrieve SSA from spectral albedo observations in the NIR (Dominé et al., 2006; Gallet et al., 2011; Libois et al., 2015; Picard et al., 2016). By neglecting roughness, SSA retrievals are underestimated to

compensate for the albedo reduction caused by the presence of roughness. We calculated SSA retrievals for experiments C and D at each $\Delta\varphi_r$ by fitting $\alpha_{sim,smooth}$ and α_{obs} acquired over the rough surfaces. Compared to measure SSA taken over the smooth surface, results demonstrate that roughness introduces a significant underestimation of the retrieved SSA, reaching 21 % for

535   the roughness features considered here. Thus, it is important to use a model considering roughness to retrieve accurate SSA from albedo observations.
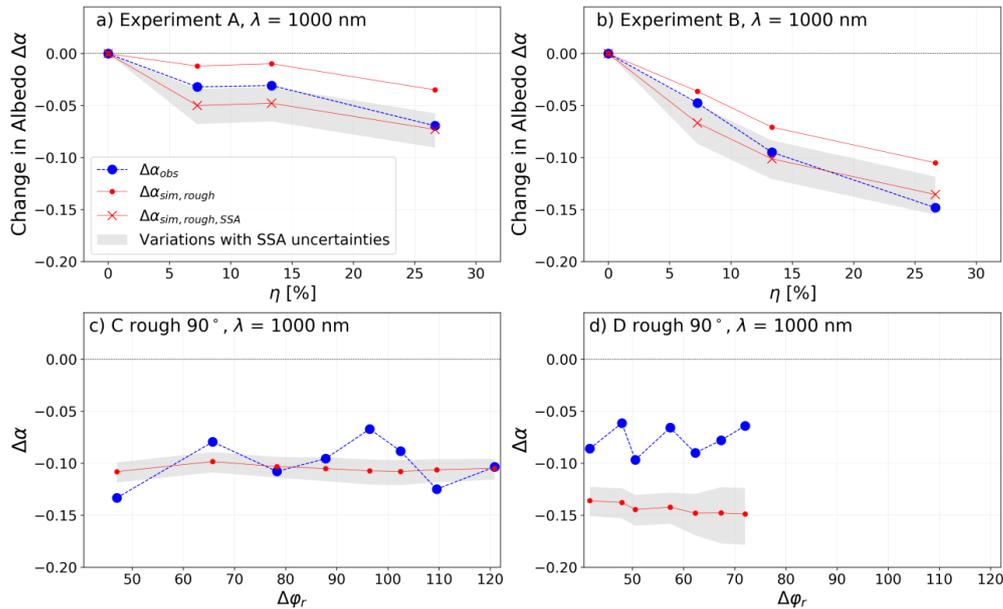
Figure 9. a) and b) are changes in albedo as a function of the η ratio at 1000 nm for experiments A and B, respectively. Blue dotted lines are $\Delta\alpha_{obs}$ ($\alpha_{obs}(\lambda, \theta_s) - \alpha_{obs}(\lambda, \theta_{s,o})$). Red dotted lines with points are $\Delta\alpha_{sim,rough}$ ($\alpha_{sim,rough}(\lambda, \theta_s) - \alpha_{sim,smooth}(\lambda, \theta_{s,o})$) obtained using a
540   constant SSA in RSRT (7.4 m^2 kg^{-1} for A and 4.5 m^2 kg^{-1} for B). Red lines with crosses are $\Delta\alpha_{sim,rough,ssa}$ ($\alpha_{sim,rough,ssa}(\lambda, \theta_s, SSA_r) - \alpha_{sim,smooth}(\lambda, \theta_{s,o}, SSA_m)$) obtained using SSA$_r$ for the smooth surface (at $\eta = 0$ %, SSA$_r$ = 9.4 m^2 kg^{-1} for A and 5.3 m^2 kg^{-1} for B) and SSA$_m$ for rough surfaces (η from 7 % to 27 %, SSA$_m$ = 7.4 m^2 kg^{-1} for A and 4.5 m^2 kg^{-1} for B). c) and d) are variations of $\Delta\alpha$ with $\Delta\varphi_r$ at 1000 nm for experiments C and D, respectively (similar to Figures 8e and 8f). $\Delta\alpha_{obs}$ and $\Delta\alpha_{sim,rough}$ are the observed and simulated albedo differences between the rough and the smooth surfaces at $\Delta\varphi_r$. Grey shades represent the range of $\Delta\alpha$ obtained by
545   varying the SSA by ± 10% in RSRT simulations.

4.2.2 Sensitivity to the surface slope

The impact of slope uncertainties is explored by varying the slope by ± 1° for simulations over the rough surfaces for experiments C and D at 1000 nm (Sect. 3.3). Obtained values range within the grey shade shown in Figure 10. The albedo sensitivity to the slope depends of the slope aspect φ_n, with respect to the solar azimuthal angle φ_s, since the aspect controls
550   the change in the incident angle $(\widetilde{\theta_s})$ relative to Θ_s. Eq. (6) and (7) show that slopes have no impacts on albedo if the aspect is perpendicular to the solar azimuthal angle ([$\varphi_s - \varphi_n$] = 90° or 270°), while impacts change rapidly when φ_n becomes parallel to φ_s ([$\varphi_s - \varphi_n$] = 0° or 180°). In addition, between [$\varphi_s - \varphi_n$] = 0° or 180°, the albedo sensitivity to the slope is opposite whether the surface is smooth or rough. Indeed, over a tilted smooth surface, if the slope aspect is opposite to that of the sun ($\varphi_s - \varphi_n$ = 180°), the surface experiences a larger effective incident angle relative to a flat smooth surface, i.e. a higher albedo. Conversely,
555   over a tilted rough surface with roughness orientation perpendicular to the sun and $\varphi_s - \varphi_n$ = 180°, roughness sides facing the sun experience a lower effective incident angle relative to a flat rough surface, leading to a lower albedo. Fig. 10b illustrates this point for experiment D rough 90°: the albedo sensitivity is twice as strong when the slope direction is closer to 180° ([$\varphi_s - \varphi_n$] = - 150°) than when it gets closer to 90° ([$\varphi_s - \varphi_n$] = - 120°). Note that this experiment has low SSA, leading to a strong

sensitivity to a change of the incident angle (Eq. (4)). Therefore, for low SSA, the impact of roughness on albedo is accentuated when the slope direction is opposite to the sun, and attenuated when the slope is facing the sun.

In experiment C (Fig. 10a), the albedo is highly sensitive to slope uncertainties (variations of 0.05-0.15). However, due to high SSA there is a low albedo sensitivity to the $\varphi_s - \varphi_n$ angle (the effective angle effect is negligible). Therefore, the observed albedo sensitivity may be explained by a larger effect of multiple reflections, accentuated by the fact that Θ_s is particularly large for this experiment (> 60°).

To sum up, we have shown that the albedo sensitivity to roughness is larges when the SSA is low (< 10 m² kg⁻¹), when roughness features are perpendicular to the sun, and when the surface aspect is facing away the sun. The impact of roughness if strongly linked to SSA values which affect: 1) the effective angle effect, since the decrease of the incident angle on roughness sides facing the sun has more consequences on the albedo when SSA is low (high absorption), 2) the impact of multiple reflections, which is larger when the probability of a photon to be absorbed or reflected is well balanced. To accurately quantify roughness effects, it is crucial to measure SSA regularly (a small variation may overlap the roughness effects) and to determine the slope. In our experiments C and D, where SSA was measured at each albedo acquisition, we have shown that even considering uncertainties of ± 10 % of SSA and of ± 1° of slopes, roughness effects are significant and cause at least an albedo decrease of 0.06 in experiment C rough 90°, and of 0.11 in experiment D rough 90°, at 1000 nm.
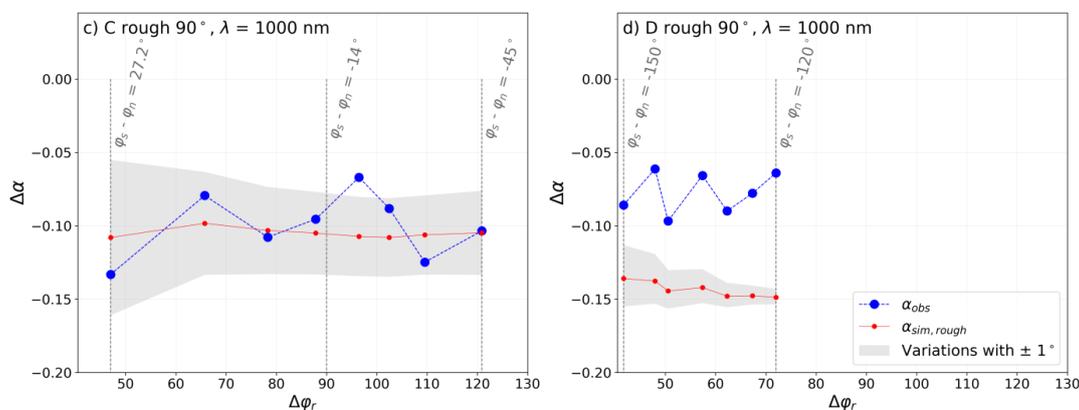
Figure 10. Same as Figure 9c and 9d, except that the grey shades represent the range of $\Delta\alpha$ obtained by varying the slope by ± 1° in RSRT simulations, for a) experiment C rough 90°, and b) D rough 90°. φ_n is the aspect of the slope and φ_s is the solar azimuthal angle, separately given in Table 1. Vertical black lines indicates [φ_s - φ_n] angles at the beginning and at the end of experiments (and at $\Delta\varphi_r$ =90° for experiment C).

4.3 Analysis of the two roughness effects

The two processes introduced by surface roughness are decoupled using RSRT to better characterise roughness effects as a function of snow properties and illumination conditions.

4.3.1 Effective angle effect

To simulate the effective angle effect, we count all photons that have not been absorbed after the first hit. RSRT is run at 1000 nm with a KZ04 configuration, and we sum the total upward and downward intensity considering one hit only. Simulations are performed for various θ_s and $\Delta\varphi_r$. The initial conditions of the A-η27% experiment without slope and under direct sunlight are used. Roughness shapes are rectangular and the SSA is low (7.4 m² kg⁻¹), which lead to a maximal effect of incident angle variations.

Figures 11a and 11b show the simulated $\Delta\alpha_{sim,rough}$ ([rough-smooth] with similar illumination) as a function of θ_s and $\Delta\varphi_r$.

590 The Lambertian configuration yields a constant albedo, as expected (no angle dependence). The albedo decreases of 0.04 due to shadow areas that receive less radiations. With the KZ04 configuration, Fig. 11a and 11b shows that the effective angle effect is strongly linked to illumination conditions. Firstly, when $\theta_s > 50°$, the model predicts a strong drop in albedo (Fig. 11a). With rectangular roughness shapes, the local incident angle of photons hitting the vertical sides facing the sun is lower than that of a smooth surface when $\theta_s > 45°$ if $\Delta\varphi_r = 90°$. Thus, photons penetrate deeply in the snowpack before being

595 eventually redirected upward, which conduces to a stronger decrease in albedo relative to a smooth surface. Conversely, when $\theta_s < 50°$, the effective incident angle is higher over roughness sides facing the sun compared to that of a smooth surface. It leads to an increase in albedo, and this is why $\Delta\alpha$ is higher with the KZ04 configuration than with the Lambertian configuration when $\theta_s < 50°$ (Fig. 11a). Hence, the reduction in albedo depends on the slope of roughness sides (i.e. their shapes). Fig. 11a also illustrates that in presence of roughness, albedo decreases more rapidly with θ_s at large values of θ_s. Therefore, surface

600 roughness play a more important role at grazing angle (large θ_s). Moreover, our results show that the effects of roughness becomes negligible at 1000 nm when $\theta_s < 30°$. The albedo decrease caused by the effective angle effect only is of 0.04 for experiment A-$\eta27\%$, when $\theta_s = 63°$ (Fig. 11a, [Lambert – KZ04]). Secondly, by changing the incidence angle, the roughness orientation also plays an important role (Fig. 11b). The reduction in albedo caused by the effective angle effect goes from 0 when $\Delta\varphi_r = 0°$ to 0.09 when $\Delta\varphi_r = 90°$ for experiment A.

605 To sum up, the albedo decrease due to the effective angle effect becomes rapidly stronger with θ_s at large θ_s ($\theta_s > 50°$) and when $\Delta\varphi_r = 90°$. In experiment A, the model predicts a decrease in albedo of 0.7 when $\theta_s = 80°$, caused by the effective angle effect only, i.e a drop 75% stronger compared to that of $\theta_s = 63°$. Therefore, it is necessary to account for the intrinsic BRDF of the snow to simulate realistic albedo over rough surfaces, in particular in Polar Regions where θ_s is high.
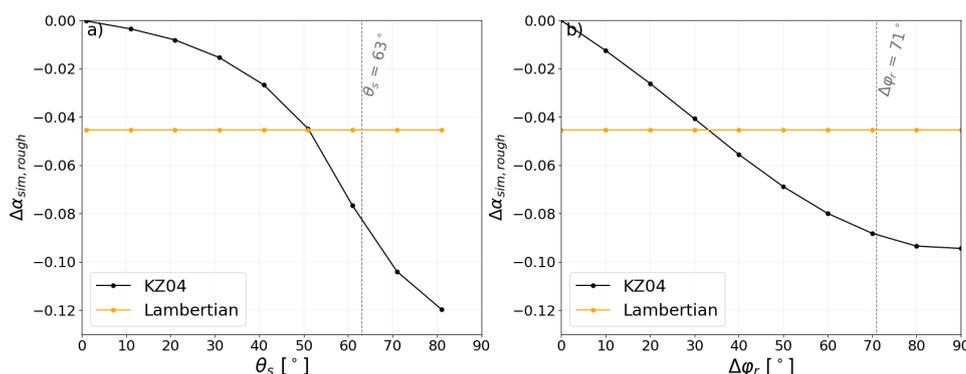
610 **Figure 11. Variations of $\Delta\alpha_{sim,rough}$ ([rough-smooth] at same illumination) simulated with RSRT at 1000 nm with the initial condition of the experiment A-$\eta27\%$, without slope as a function of a) θ_s (in degrees) and a constant $\Delta\varphi_r = 71°$; and b) $\Delta\varphi_r$ and a constant $\theta_s = 63°$. Simulations are performed with the Lambertian configuration (in orange) and the KZ04 configuration (in black). Vertical dotted lines indicate the initial condition of the experiment A-$\eta27\%$ (Table 1).**

4.3.2 Multiple reflections

615 RSRT is run by varying SSA values with the KZ04 configuration and under diffuse sunlight to simulate the trapping effect of photons only (for the A-$\eta27\%$ experiment, Sect. 3.3). Simulations are performed over a smooth and a rough surface to compute $\Delta\alpha_{sim,rough}$. Results are shown in Figure 12 as a function of SSA. The impact of multiple reflections is higher for SSA between 8 m² kg⁻¹ and 14 m² kg⁻¹, with a maximum effect at SSA = 9 m² kg⁻¹. For the experiment A-$\eta27\%$, the measured SSA is of 7.4 m² kg⁻¹, and it induces a simulated albedo equal to 0.6 at 1000 nm. Fig. 12 shows that at SSA = 7.4 m² kg⁻¹, $\Delta\alpha_{sim,rough}$

620 decreases of 0.035 with multiple reflections, which is significant. The impact of multiple reflections is larger for intermediate values of albedo since photons have the same probability to be absorbed or reflected at each collision. Fig. 12 also illustrates

that multiple reflections are less sensitive at large SSA, as discussed in Sect. 4.2. Hence, it leads to albedo close to 1 and the absorption is too low to trap the photons. Similar results were found in the literature (O'Rawe, 1991; Warren et al., 1998).

625   Therefore, for the experiment A-$\eta 27\%$, we predict that albedo decreases by 0.04 with multiple reflections and by 0.04 due to a change of the incidence angle, i.e. a total albedo decrease of 0.08 due to the presence of surface roughness. Effective angle effects increase with large θ_s and low SSA, while the impact of multiple reflections becomes larger when SSA correspond to intermediate value of albedo in the near-infrared wavelengths. Both effects are stronger when the roughness orientation is perpendicular to the sun.
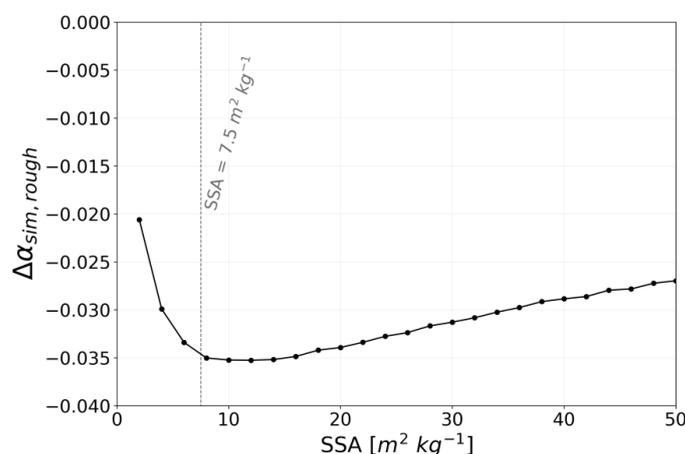
630

Figure 12. $\Delta\alpha_{sim,rough}$ **variations as a function of SSA (m² kg⁻¹). RSRT simulations are computed with the KZ04 configuration at λ=1000 nm, with the initial conditions of the experiment A-$\eta 27\%$ (rectangular shapes, θ_s = 63°, $\Delta\varphi_r$ =71°, without slope, Table 1). The vertical dotted lines indicates the measured SSA (7.4 m² kg⁻¹).**

4.4 Impact on the radiative balance

635   In this study, the observed albedo change due to the presence of surface roughness may seem low, of the order of a few percent. The decrease in albedo impacts the radiative balance by increasing the proportion of absorbed energy, estimated with the net short wave radiation (SW$_{net}$). To illustrate the importance of such an albedo decrease on the radiative balance, we compute SW$_{net}$ using RSRT with the simple approach described in the following. The net short wave radiation in the 0.35 - 4 μm range (in W m⁻²) is estimated with Eq. (17):

640 $$SW_{net} = \int_{0.3\mu m}^{4\,\mu m}(1 - \alpha_{dir}(\lambda,\theta_s))Irr_{dir}(\lambda)d\lambda + \int_{0.3\mu m}^{4\,\mu m}(1 - \alpha_{diff}(\lambda))Irr_{diff}(\lambda)d\lambda \qquad [17],$$

where $\alpha_{dir}(\lambda,\theta_s)$ and $\alpha_{diff}(\lambda)$ are the direct and diffuse albedo, and $Irr_{dir}(\lambda)$ and $Irr_{diff}(\lambda)$ the direct and diffuse solar spectral irradiance (W m⁻² μm⁻¹) computed with the Santa Barbara DISORT Atmospheric Radiative Transfer (SBDART, Ricchiazzi et al., 1998). SBDART is an atmospheric model computing radiative transfer within the Earth's atmosphere and at the surface, in clear-sky (direct illumination) and cloudy conditions (diffuse illumination).

645   The net short wave radiation is estimated with Eq. (17) over the C smooth and C rough 90° surfaces using $\alpha_{sim,smooth}$ and $\alpha_{sim,rough}$, respectively, at θ_s = 68°. SBDART is run with a mid-latitude winter atmospheric profile, at 1729 meters high (elevation of the site of experiment C), and at noon. Between these smooth and rough surfaces, the decrease in broadband albedo is equal to 0.05, resulting to an increase of the SW$_{net}$ from 15 W m⁻² to 27 W m⁻². Thus, the energy absorbed by the snowpack increases by almost a factor two (+80 %) with the presence of roughness. These results illustrate the necessity to consider surface

650   roughness in the estimation of the surface energy budget. The RSRT was evaluated with artificial roughness here, and further work will logically concern natural rough surfaces.

6 Summary and perspectives

Four controlled experiments using artificial roughness fields with various geometrical characteristics (fraction of roughness features, orientation, etc.) were studied. Our observations show that the presence of macroscopic surface roughness

655   significantly decrease snow albedo. More specifically:

-    Even a low fraction of roughness features ($\eta = 7\%$) causes a detectable albedo decrease up to 0.02 at 1000 nm relative to a smooth surface,

-    For higher fractions ($\eta = 27\%$ and 63%), and when the roughness orientation is perpendicular to the sun, the decrease ranges between $0.03 - 0.05$ at 700 nm and of $0.07 - 0.10$ at 1000 nm. The impact is 20% lower when the orientation

660   is parallel to the sun.

-    At low SSA ($10 \ m^2 \ kg^{-1}$), the albedo sensitivity to surface roughness is twice as large at 1000 nm (NIR) than at 700 nm (visible) due to the higher intrinsic absorption of the snow.

We developed a new model to account for surface roughness in snow albedo simulations. RSRT considers both the 3-D geometric effects introduced by roughness and snow optical properties using a Monte Carlo photon transport algorithm. By

665   considering roughness, albedo simulations are improved by a factor 2 compared to those assuming a smooth surface (RMSD of 0.03 at 700 nm and 0.04 at 1000 nm).

Using RSRT, we analysed how the contributions usually affecting albedo interact with the effects of roughness.

Firstly, we investigated the impact of SSA and slope uncertainties in our roughness analysis. The amplitude of roughness effects is insensitive to SSA variations at high SSA. On the contrary, at low SSA, a SSA decrease of 50 % induces the same

670   reduction in albedo that the one due to the presence of roughness. Hence, the albedo decrease due to the presence of roughness is drastically accentuated when SSA is low ($< 10 \ m^2 \ kg^{-1}$) and when the roughness orientation is perpendicular to the sun. This is explained by 1) when the sun elevation is low, the reduction of the local incident angle of roughness sides facing the sun has more consequences on the albedo when SSA is low (higher absorption of photons), and 2) the impact of multiple reflections is larger when the probability of a photon to be absorbed or reflected is well balanced, which is mainly controlled by a low

675   SSA in the NIR (albedo ~ 0.6). In addition, the overall slope of the rough surface changes the local incident angle and accentuates roughness effects when the surface aspect is facing away the sun. Therefore, to accurately quantify the effects of roughness, it is necessary to know SSA variations when albedo measurements are acquired and the slope of the surface.

Secondly, the two processes governing roughness effects were quantified separately with RSRT. We showed that the albedo decrease due to the effective angle effect becomes rapidly stronger with θ_s at large θ_s ($\theta_s > 50°$) and when $\Delta\varphi_r = 90°$. For

680   instance, the effective angle effect may cause a reduction in albedo 75% stronger when θ_s goes from 63° to 80° for roughness shapes considered here. The impact of multiple reflections is larger for SSA between $8 \ m^2 \ kg^{-1}$ and $14 \ m^2 \ kg^{-1}$. Thus, the impact of roughness is strongly linked to SSA, slope, the solar zenith angle and the roughness orientation. RSRT provides a useful tool to better characterize the albedo sensitivity to macroscopic surface roughness.

Roughness effects are significant and many biases are introduced by neglecting these contributions. For approaches

685   considering a smooth surface and using simulated and observed albedo to retrieve SSA, the presence of roughness causes a strong underestimation of SSA, which can be of the order of 20 % for roughness features perpendicular to the sun. Moreover, the albedo decrease leads to an increase of the absorbed energy in the snowpack. In one of our experience, we found that a decrease of the broadband albedo of 0.05 causes +80 % of additional net short wave radiations relative to a smooth surface. This result highlights the necessity to take into account the roughness effects to compute the surface energy budget. RSRT was

690   evaluated on meter-scale artificial roughness. In further work it will be applied both for natural roughness and at a larger scale in complex terrain (mountainous area).

Author Contributions: Fanny Larue, Ghislain Picard, and Laurent Arnaud contributed to the conceptualization and design of the work. All authors contributed to the observation acquisition, analysis, and interpretation of data. Ghislain Picard wrote
695   RSRT, Fanny Larue led the analysis and wrote the manuscript, and all the authors contributed to revisions of the manuscript.

Aknowledgements. This project was supported under the EAIIST project, with the financial contribution of the Institut Polaire Français Paul-Emile Victor (IPEV), the Agence Nationale de la Recherche (ANR programs 1-JS56-005-01 MONISNOW and ANR-16-CE01-0006 EBONI), Equipex CLIMCOR, the Centre de Carottage et de Forage National (C2FN), the Station Alpine
700   Joseph Fourier (SAJF) and the Centre Nationnal d'Etudes Spatiales (CNES). CNRM-CEN and IGE are part of Labex OSUG@2020 (investissement d'avenir – ANR10 LABX56). The authors would like to thank Bertrand Cluzet (Centre d'Études de la Neige, Météo-France) for his help during the field campaigns.

Data availability:

705   The albedo observations and auxiliary data will be assembled in an open datatset to be released on https://persyval-platform.univ-grenoble-alpes.fr after the review process.

Competing interests. The authors declare that they have no conflict of interest.

References

710   Arnaud, L., Picard, G., Champollion, N., Domine, F., Gallet, J. C., Lefebvre, E., and Barnola, J. M.: Measurement of vertical profiles of snow specific surface area with a 1 cm resolution using infrared reflectance: instrument description and validation. *Journal of Glaciology,* 57(201), 17–29. https://doi.org/10.3189/002214311795306664, 2011.

Atlaskina, K., Berninger, F., and De Leeuw, G.: Satellite observations of changes in snow-covered land surface albedo during spring in the Northern Hemisphere. *The Cryosphere,* 9, 1879–1893. https://doi.org/10.5194/tc-9-1879-2015, 2015.

715   Brock, B. W., Willis, I. C., & Sharp, M. J.: Measurement and parameterization of albedo variations at Haut Glacier d'Arolla, Switzerland. *Journal of Glaciology*, 46(155), 675-688. https://doi.org/10.3189/172756500781832675, 2000.

Carroll, J. J., and Fitch, B. W.: Effects of solar elevation and cloudiness on snow albedo at the South Pole. *Journal of Geophysical Research,* 86(C6), 5271. https://doi.org/10.1029/JC086iC06p05271, 1981.

Cathles, L. M., Abbot, D. S., Bassis, J. N., and MacAyeal, D. R.: Modelling surface-roughness/solar-ablation feedback:
720   Application to small-scale surface channels and crevasses of the Greenland ice sheet. *Annals of Glaciology, 52*(59), 99–108. https://doi.org/10.3189/172756411799096268, 2011.

Cathles, L. M., Abbot, D. S., and MacAyeal, D. R.: Intra-surface radiative transfer limits the geographic extent of snow penitents on horizontal snowfields. *Journal of Glaciology*, 60(219), 147-154. https://doi.org/10.3189/2014JoG13J124, 2014.

725   Corbett, J., and Su, W.: Accounting for the effects of sastrugi in the CERES clear-sky Antarctic shortwave angular distribution models. *Atmos. Meas. Tech*, 8, 3163–3175. https://doi.org/10.5194/amt-8-3163-2015, 2015.

Domine, F., Salvatori, R., Legagneux, L., Salzano, R., Fily, M., and Casacchia, R.: Correlation between the specific surface area and the short-wave infrared (SWIR) reflectance of snow. *Cold Regions Science and Technology*, 46(1), 60–68. https://doi.org/10.1016/j.coldregions.2006.06.002, 2006

730   Dumont, M., Arnaud, L., Picard, G., Libois, Q., Lejeune, Y., Nabat, P., and Morin, S.: In situ continuous visible and near-infrared spectroscopy of an alpine snowpack. *The Cryosphere*, 11(3), 1091–1110. https://doi.org/10.5194/tc-11-1091-2017, 2017.

Filhol, S., and Sturm, M.: Snow bedforms: a review, new data, and a formation model. *Journal of Geophysical Research: Earth Surface*, 120, 1645–1669. https://doi.org/10.1002/2015JF003529, 2015.

735   Flanner, M. G., Zender, C. S., Hess, P. G., Mahowald, N. M., Painter, T. H., Ramanathan, V., and Rasch, P. J.: Sprintime warming and reduced snow cover from carbonaceous particles. *Atmos. Chem. Phys.*, 9, 2481–2497, 2009.

Fréville, H., Brun, E., Picard, G., Tatarinova, N., Arnaud, L., Lanconelli, C., Reijmer, C., and Van Den Broeke, M.: Using MODIS land surface temperatures and the Crocus snow model to understand the warm bias of ERA-Interim reanalyses at the surface in Antarctica, *The Cryosphere*, 8, 1361-1373, https://doi.org/10.5194/tc-8-1361-201, 2014.

740   Gallet, J. C., Domine, F., Zender, C. S., and Picard, G.: Measurement of the specific surface area of snow using infrared reflectance in an integrating sphere at 1310 and 1550 nm. *The Cryosphere*, 3(2), 167–182. https://doi.org/10.5194/tc-3-167-2009, 2009.

Gallet, J. C., Domine, F., Arnaud, L., Picard, G., and Savarino, J.: Vertical profile of the specific surface area and density of the snow at Dome C and on a transect to Dumont D'Urville, Antarctica - Albedo calculations and comparison to remote

745   sensing products. *The Cryosphere*, 5(3), 631–649. https://doi.org/10.5194/tc-5-631-2011, 2011.

Genthon, C.: Antarctic climate modelling with general circulation models of the atmosphere. *Journal of Geophysical Research,* 99(D6), 12953. https://doi.org/10.1029/94JD00574, 1994.

Greenwood, J.: The correct and incorrect generation of a cosine distribution of scattered particles for Monte-Carlo modelling of vacuum systems. *Vacuum*, 67(2), 217–222. https://doi.org/10.1016/S0042-207X(02)00173-2, 2002.

750   Grenfell, C., Warren, S. G., and Mullen, C.: Reflection of solar radiation by the Antarctic snow surface at ultraviolet, visible, and near-infrared wavelengths. *Journal of Geophysical Research.* 99(9), 18669–18684, 1994.

Grenfell, T. C., and Maykut, G. A.: The optical properties of ice and snow in the Arctic Basin. Journal of Glaciology, 18(80), 445-463. https://doi.org/10.3189/s0022143000021122, 1977.

Hudson, S. R., and Warren, S. G.: An explanation for the effect of clouds over snow on the top-of-atmosphere bidirectional

755   reflectance. *J. Geophys. Res,* 112. https://doi.org/10.1029/2007JD008541, 2007.

Iwabuchi, H.: Efficient Monte Carlo Methods for Radiative Transfer Modeling. J*ournal of the Atmospheric Sciences*, 63, 2324. Retrieved from https://journals.ametsoc.org/doi/pdf/10.1175/JAS3755.1, 2006.

Ize, T.: Robust BVH Ray Traversal. *Journal of Computer Graphics Techniques*, 2(2), 12–27, 2013.

Kaempfer, T. U., Hopkins, M. A., and Perovich, D. K.: A three-dimensional microstructure-based photon-tracking model of

760   radiative transfer in snow. *Journal of Geophysical Research*, 112(D24), D24113. https://doi.org/10.1029/2006JD008239, 2007.

Kokhanovsky, A. A.: A semianalytical cloud retrieval algorithm using backscattered radiation in 0.4–2.4 μm spectral region. *Journal of Geophysical Researc*h, 108(D1), 1–19. https://doi.org/10.1029/2001jd001543, 2003.

Kokhanovsky, A. A.: Spectral reflectance of solar light from dirty snow: a simple theoretical model and its validation. *The*

765   *Cryosphere*, 7, 1325–1331. https://doi.org/10.5194/tc-7-1325-2013, 2013.

Kokhanovsky, A. A., and Zege, E. P.: Scattering optics of snow. *Applied Optics*, 43(7), 1589–1602. https://doi.org/ 10.1364/AO.43.001589, 2004.

Kuchiki, K., Aoki, T., Niwano, M., Motoyoshi, H., and Iwabuchi, H.: Effect of sastrugi on snow bidirectional reflectance and its application to MODIS data. *Journal of Geophysical Research Atmospheres*, 116(18), 1–15.

770   https://doi.org/10.1029/2011JD016070, 2011.

Kuhn, M.: Bidirectional Reflectance of Polar and Alpine Snow Surfaces. *Annals of Glaciology,* 6, 164–167. https://doi.org/10.3189/S0260305500010259, 1985.

Lafortune, E.: Mathematical Models and Monte Carlo Algorithms for Physically Based Rendering. https://doi.org/10.1.1.38.3626, 1995.

775   Leroux, C., and Fily, M.: Modeling the effect of sastrugi on snow reflectance. *Journal of Geophysical Research*, 103(E11), 25779. https://doi.org/10.1029/98JE00558, 1998.

L'Hermitte, S., Abermann, J., and Kinnard, C.: Albedo over rough snow and ice surfaces. *The Cryosphere*, 8(3), 1069–1086. https://doi.org/10.5194/tc-8-1069-2014, 2014.

Libois, Q., Picard, G., France, J. L., Arnaud, L., Dumont, M., Carmagnola, C. M., and King, M. D.: Influence of grain shape on light penetration in snow. *The Cryosphere*, 7, 1803–1818. https://doi.org/10.5194/tc-7-1803-2013, 2013.

Libois, Q., Picard, G., Dumont, M., Arnaud, L., Sergent, C., Pougatch, E., Sudul, M., and Vial, D.: Experimental determination of the absorption enhancement parameter of snow, J. Glaciol., 60, 714–724, https://10.3189/2014jog14j015, 2014b.

Libois, Q., Picard, G., Arnaud, L., Dumont, M., Lafaysse, M., Morin, S., and Lefebvre, E.: Summertime evolution of snow specific surface area close to the surface on the Antarctic Plateau. *The Cryosphere*, 9, 2383–2398. https://doi.org/10.5194/tc-9-2383-2015, 2015.

Mondet, J., and Fily, M.: The reflectance of rough snow surfaces in Antarctica from POLDER/ADEOS remote sensing data. *Geophysical Research Letters.* 26(23), 3477–3480. https://doi.org/10.1029/1999GL010913, 1999.

Naegeli, K., and Huss, M.: Sensitivity of mountain glacier mass balance to changes in bare-ice albedo. *Annals of Glaciology*, 58(75pt2), 119–129. https://doi.org/10.1017/aog.2017.25, 2017.

Naaim-Bouvet, F., Naaim, M., Bellot, H., and Nishimura, K.: Wind and drifting-snow gust factor in an Alpine context. Annals of Glaciology, 52(58), 223–230. https://doi.org/10.3189/172756411797252112, 2011.

Negi, H. S., Kokhanovsky, A., and Perovich, D. K.: Application of asymptotic radiative transfer theory for the retrievals of snow parameters using reflection and transmission observations. *The Cryosphere Discussions,* 5(2), 1239–1262. https://doi.org/10.5194/tcd-5-1239-2011, 2011.

O'Rawe, P.: Monte Carlo models for the reflection of sunlight from rough snow surfaces: suncups and sastrugi. M.S Thesis - University of Washington. Retrieved from https://www.researchgate.net/publication/34100391, 1991.

Oaida, C. M., Xue, Y., Flanner, M. G., Skiles, S. M. K., De Sales, F., and Painter, T. H.: Improving snow albedo processes in WRF/SSiB regional climate model to assess impact of dust and black carbon in snow on surface energy balance and hydrology over western U.S. *Journal of Geophysical Research,* 120(8), 3228–3248. https://doi.org/10.1002/2014JD022444, 2015.

Painter, T. H., Deems, J. S., Belnap, J., Hamlet, A. F., Landry, C. C., & Udall, B.: Response of Colorado River runoff to dust radiative forcing in snow. *Proceedings of the National Academy of Sciences*, 107(40), 17125–17130. https://doi.org/10.1073/pnas.0913139107, 2010.

Pfeffer, W. T., and Bretherton, C. S.: The effect of crevasses on the solar heating of a glacier surface. *IAHS Red Book*, (170), 191–206, 1987.

Picard, G., Domine, F., Krinner, G., Arnaud, L., and Lefebvre, E.: Inhibition of the positive snow-albedo feedback by precipitation in interior Antarctica, *Nature Clim. Change,* 2, 795–798, doi:10.1038/nclimate1590, 2012.

Picard, G., Libois, Q., Arnaud, L., Verin, G., and Dumont, M.: Development and calibration of an automatic spectral albedometer to estimate near-surface snow SSA time series. *The Cryosphere*, 10, 1297–1316. https://doi.org/10.5194/tc-10-1297-2016, 2016.

Ricchiazzi, P., Yang, S., Gautier, C., and Slowle, D.: SB DART: A Research and Teaching Software Tool for Plane-Parallel Radiative Transfer in the Earth's Atmosphere. *Bull. Amer. Meteor. Soc*., 79, 2101–2114. Retrieved from https://doi.org/10.1175/1520-0477(1998)079%3C2101:SARATS%3E2.0.CO;2, 1998.

Schaepman-Strub, G., Schaepman, M. E., Painter, T. H., Dangel, S., and Martonchik, J. V.: Reflectance quantities in optical remote sensing-definitions and case studies. Remote Sensing of Environment, 103(1), 27–42. https://doi.org/10.1016/j.rse.2006.03.002, 2006.

Sicart, J. E., Ribstein, P., Wagnon, P., and Brunstein, D.: Clear-sky albedo measurements on a sloping glacier surface: A case study in the Bolivian Andes. *Journal of Geophysical Research Atmospheres,* 106(D23), 31729–31737. https://doi.org/10.1029/2000JD000153, 2001.

Skiles, S. M., Flanner, M., Cook, J. M., Dumont, M., and Painter, T. H.: Radiative forcing by light-absorbing particles in snow. Nature Climate Change, 8(11), 964–971. https://doi.org/10.1038/s41558-018-0296-5, 2018.

Wang, X., Pu, W., Ren, Y., Zhang, X., Zhang, X., Shi, J., and Chen, Q.: Observations and model simulations of snow albedo reduction in seasonal snow due to insoluble light-absorbing particles during 2014 Chinese survey. *Atmos. Chem. Phys*, 17, 2279–2296. https://doi.org/10.5194/acp-17-2279-2017, 2017.

825 Warren, S. G.: Optical properties of snow. *Reviews of Geophysic*s, Vol. 20, pp. 67–89. https://doi.org/10.1029/RG020i001p00067, 1982.

Warren, S. G., Brandt, R. E., and O'Rawe Hinton, P.: Effect of surface roughness on bidirectional reflectance of Antarctic snow. *Journal of Geophysical Research*: Planets, 103(E11), 25789–25807. https://doi.org/10.1029/98JE01898, 1998.

Wendler, G., and Kelley, J.: On the albedo of snow in Antarctica: a contribution to I.A.G.O.*. *Journal of Glaciology*, 34(116). 830 Retrieved from https://www.igsoc.org:8080/journal/34/116/igs_journal_vol34_issue116_pg19-25.pdf, 1988.

Wuttke, S., Seckmeyer, G., and König-Langlo, G.: Measurements of spectral snow albedo at Neumayer, Antarctica. *In Annales Geophysicae* (Vol. 24). Retrieved from http://lap.physics.auth.gr/, 2006.

Zhuravleva, T. B., and Kokhanovskii, A. A.: Influence of horizontal inhomogeneity on albedo and absorptivity of snow cover. *Russian Meteorology and Hydrology,* 35(9), 590–595. https://doi.org/10.3103/S1068373910090025, 2010.

835 Zhuravleva, T. B., and& Kokhanovsky, A. A.: Influence of surface roughness on the reflective properties of snow. *Journal of Quantitative Spectroscopy and Radiative Transfer*, 112(8), 1353–1368. https://doi.org/10.1016/J.JQSRT.2011.01.004, 2011.